Lithos 268–271 (2017) 399–417

Contents lists available at ScienceDirect

Lithos

journal homepage: www.elsevier.com/locate/lithos

The distribution, geochronology and geochemistry of early Paleozoic granitoid plutons in the North Altun orogenic belt, NW China: Implications for the petrogenesis and tectonic evolution

Ling-Tong Meng [a,*], Bai-Lin Chen [a,*], Ni-Na Zhao [b,c], Yu Wu [a], Wen-Gao Zhang [a], Jiang-Tao He [a,c], Bin Wang [c], Mei-Mei Han [a,c]

[a] Institute of Geomechanics, Chinese Academy of Geological Sciences, Beijing 100081, China
[b] Shaanxi Geological Exploration Institute of Geology and Mine Bureau, Xi'an 710065, China
[c] School of Earth Sciences and Resources, China University of Geosciences (Beijing), Beijing 100083, China

ARTICLE INFO

Article history:
Received 19 February 2016
Accepted 22 October 2016
Available online 29 October 2016

Keywords:
North Altun orogenic belt
Early Palezoic granitoids
Geochemistry
Zircon geochronology and Hf isotopes
Flat-slab subduction
Subduction angle change

ABSTRACT

Abundant early Paleozoic granitoid plutons are widely distributed in the North Altun orogenic belt. These rocks provide clues to the tectonic evolution of the North Altun orogenic belt and adjacent areas. In this paper, we report an integrated study of petrological features, U–Pb zircon dating, in situ zircon Hf isotope and whole-rock geochemical compositions for the Abei, 4337 Highland and Kaladawan Plutons from north to south in the North Altun orogenic belt. The dating yielded magma crystallization ages of 514 Ma for the Abei Pluton, 494 Ma for the 4337 Highland Pluton and 480–460 Ma for the Kaladawan Pluton, suggesting that they are all products of oceanic slab subduction because of the age constraint. The Abei monzogranites derived from the recycle of Paleoproterozoic continental crust under low-pressure and high-temperature conditions are products of subduction initiation. The 4337 Highland granodiorites have some adakitic geochemical signatures and are sourced from partial melting of thickened mafic lower continental crust. The Kaladawan quartz diorites are produced by partial melting of mantle wedge according to the positive $\varepsilon_{Hf}(t)$ values, and the Kaladawan monzogranite-syenogranite are derived from partial melting of Neoproterozoic continental crust mixing the juvenile underplated mafic material from the depleted mantle. These results, together with existing data, provide significant information about the evolution history of oceanic crust subduction during the 520–460 Ma. The initiation of subduction occurred during 520–500 Ma with formation of Abei Pluton; subsequent transition from steep-angle to flat-slab subduction at ca.500 Ma due to the arrival of buoyant oceanic plateaus, which induces the formation of 4337 Highland Pluton. With ongoing subduction, the steep-angle subduction system is reestablished to cause the formation of 480–460 Ma Kaladawan Pluton. Meanwhile, it is this model that account for the temporal–spatial distribution of these early Paleozoic magmatic rocks in the North Altun orogenic belt.

1. Introduction

It is the "subduction factory" that is famous for the abundant magmatic activity caused by the intense interaction between the crust and mantle (Tatsumi and Kogiso, 2003), so the granitoids play an important role on the rebuilding the subduction history (e.g. Barbarin, 1999; Yang et al., 2012; Zhao et al., 2008). Meanwhile, the distribution and characteristics of magmatic rocks at an active continental margin are influenced by the subduction angle of the oceanic slab, the convergence rate between two plates and the presence of aseismic ridges or oceanic plateaus (Condie, 2005a; Wilson, 2007).

In a steep-angle subduction system, trench retreat, oceanic slab rollback and lithospheric extension of the fore-arc region can trigger decompression melting of the continental crust to form the subduction-related peraluminous granitoids (Chen et al., 2014; Collins, 2002; Collins and Richards, 2008). However, a flat-slab subduction system in which the descending and overriding plates are more strongly coupled generates lithospheric contraction with intense compressional deformation, volcanic gaps and the retro-arc foreland basins (Condie, 2005a; Kay et al., 2005; Ramos et al., 2002; Ramos and Folguera, 2009). In this situation, the mantle wedge beneath the continental crust is so thin that crustal assimilation is significant and external fluids are able to penetrate the mantle to induce partial melting of the thickened lower continental crust (Chiaradia et al., 2009; Kay and Abbruzzi, 1996; Zhu et al., 2013). Studies of the Central–Southern Andes indicate that the subduction angle varies rather than remaining constant, and the transition from steep-angle to flat-slab subduction is caused by the intermittent subduction of buoyant oceanic plateaus (Cawood et al., 2009; Collins, 2002; Collins and Richards, 2008; Li and Li, 2007; Lister and Forster, 2009). In addition, Lister and Forster (2009)

* Corresponding authors.
E-mail addresses: tone18@sina.com (L.-T. Meng), cblh6299@263.net (B.-L. Chen).

http://dx.doi.org/10.1016/j.lithos.2016.10.022
0024-4937/© 2016 Published by Elsevier B.V.

proposed that orogenesis is typified by the repeated transition from lithospheric extension to contraction; the formation of some ore deposits is linked to this transition, such as the El Indio mineral district in the Southern Andes (Kay and Mpodozis, 2001).

The Altun orogenic belt at the northeastern margin of the Tibetan Plateau has recorded the breakup of the Rodinia supercontinent, oceanic ridge spreading, oceanic crust subduction, continental collision and orogenic collapse from the Neoproterozoic to the Paleozoic (Gehrels et al., 2003a, 2003b; Guo et al., 2005; Han et al., 2012; Sobel and Arnaud, 1999; Wang et al., 2013; Yu et al., 2013; Zhang et al., 2005, Zhang et al., 2014). And the North Altun orogenic belt (NAOB) is one structural unit in it. Numerous authors have focused on the tectonic evolution of NAOB during the Paleozoic (Fig. 1), particularly the presence of ophiolites, magmatic assemblages and high-pressure/low-temperature metamorphic rocks (HP/LT) (Han et al., 2012; Hao et al., 2006; Liu et al., 2013; Qi et al., 2005a, 2005b; Wu et al., 2002; Wu et al., 2005, 2007; Wu et al., 2016; Xiu et al., 2007; Yang et al., 2008; Zhang et al., 2005). These studies have shown that these rock assemblages formed in an active continental margin setting during the period of early Paleozoic. Although the tectonic evolution of the region is divided into three stages and it is known that subduction of oceanic crust occurred during 520–460 Ma (Gehrels et al., 2003a, 2003b; Han et al., 2012; Zhang et al., 2015), the subduction history has not yet been proposed.

In this paper we report petrological, geochemical, zircon U-Pb chronological and Lu-Hf isotopic data for the early Paleozoic granitoids from the NAOB in order to discuss their petrogenesis and tectonic implication. We also propose a new model in which the subduction angle changed during the early Paleozoic, thereby accounting for the temporal–spatial distribution of these magmatic rocks.

2. Tectonic setting

2.1. Regional geology

The Altun orogenic belt is ~800 km long and ~150 km wide and it has been divided into four secondary tectonic units (Fig. 1a): (1) the Dunhuang Block (DB), (2) the North Altun orogenic belt (NAOB), (3) the Central Altun Block (CAB), and (4) the South Altun orogenic belt (SAOB) (Xu et al., 1999). These four tectonic units are similar with those in the Qilian Mountain (Fig. 1a), assuming 350–400 km of left lateral displacement for the Altyn Tagh fault (Ritts and Biffi, 2000; Xu et al., 1999; Zhang et al., 2015).

The Precambrian basement exposed in the DB is mainly the Neoarchean to Paleoproterozoic Aketashitage Group (Fig. 1b) which comprises various types of mafic granulite, amphibolite and granitic gneiss (Long et al., 2014; Lu et al., 2008). Lu et al. (2008) reported a 3605 ± 43 Ma inherited zircon age from the Aketashitage Group which is the oldest one found in Northwest China.

The NAOB is bounded by the Northern Altun Fault to the north within the DB (Fig. 1b). This belt is 300 km long and extends NEE-

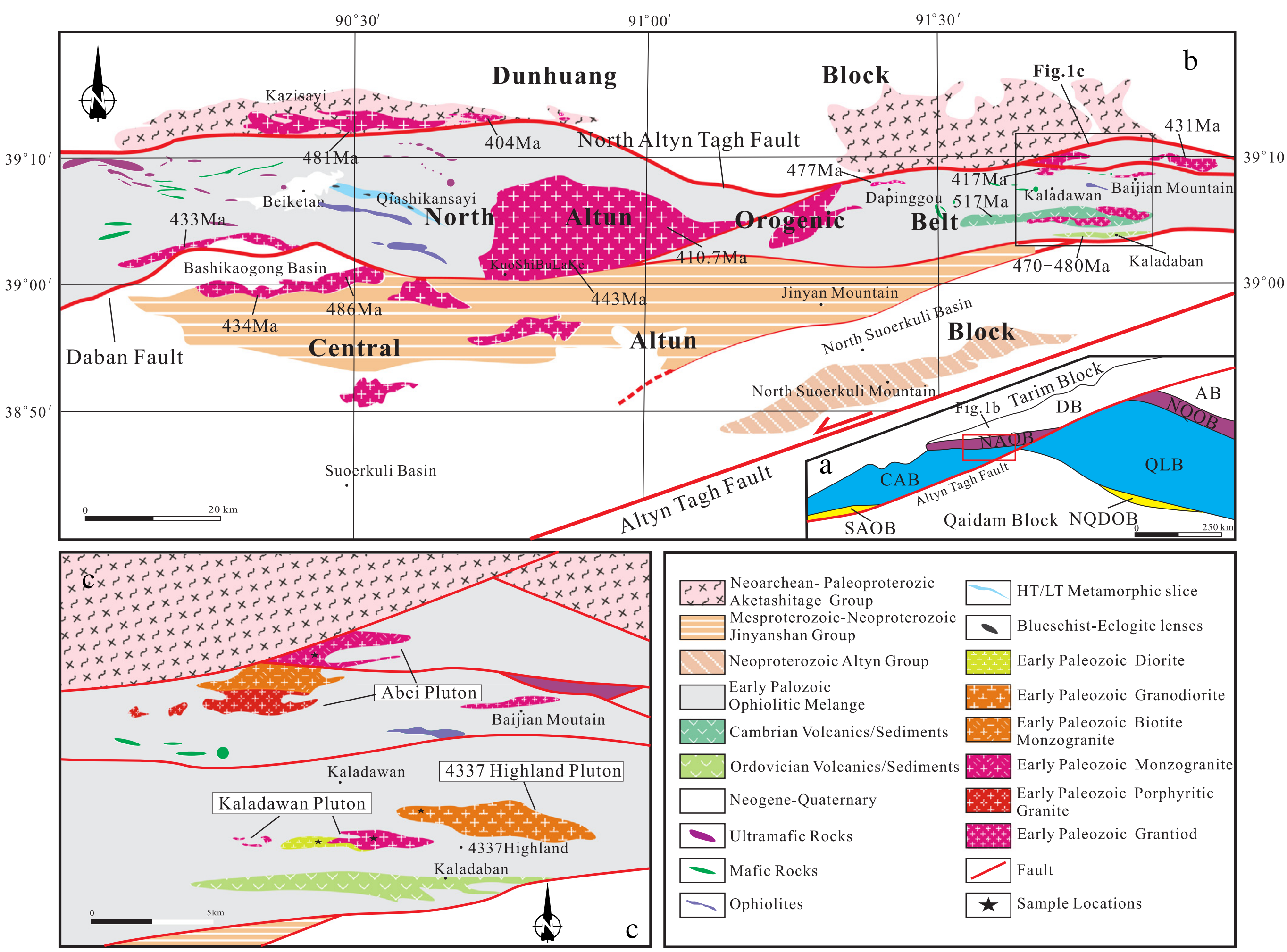

Fig. 1. (a) Geological map showing the tectonic units in the Altun Mountains and adjacent areas (after Xu et al., 1999). (b) Simplified geological map of the Altun Orogenic belt showing the distribution of Precambrian basement and early Paleozoic ultramafic rocks, volcanic rocks and magmatic rocks. (c) Geological map of the study area. The zircon U–Pb age data in (b) are from previous studies (Qi et al., 2005a, 2005b; Wu et al., 2005, 2007; Hao et al., 2006; Han et al., 2012). Abbreviation: DB = Dunhuang Block; NAOB = North Altun orogenic belt; CAB = Central Altun Block; SAOB = South Altun orogenic belt; AB = Alashan Block; NQOB = North Qilian orogenic belt; QLB = Qilian Block; NQDOB = North Qaidam orogenic belt.

SWW; it is offset by the Altyn Tagh Fault. It consists mainly of early Paleozoic ophiolites, various volcanic and granitic rocks, high-pressure eclogites and flysch sediments. Magmatic zircon dating of the Qiashikasayi ophiolites gives ages of 490–450 Ma. The geochemical characteristics of these ophiolites suggest that they were formed in a subduction setting (Liu et al., 2013; Wu et al., 2002; Xiu et al., 2007; Yang et al., 2008). The blueschists and eclogites occur as lenses surrounding the meta-pelite show a cold subduction zone with a thermal gradient of 6–8 °C/km^{-1} (Zhang and Meng, 2006); zircon dating displays the blueschists and eclogites formed between 510 and 440 Ma (Zhang et al., 2015). The magmatic rocks can be subdivided into two groups: 520–470 Ma subduction-related I-type (the magmatic rocks derived from partial melting of the igneous rocks) granitoids (Gehrels et al., 2003a, 2003b; Han et al., 2012; Qi et al., 2005a; Wu et al., 2005, 2007; Wu et al., 2016), and 440–400 Ma I- and S-type (the magmatic rocks derived from partial melting of the sedimentary rocks) anorogenic granitoids (Han et al., 2012; Meng et al., 2016; Qi et al., 2005b; Wu et al., 2005, 2007). According to these rock assembles, Zhang et al. (2015) proposed that the NAOB is an accretionary orogenic belt that has both a HP/LT belt and a high-temperature magmatic arc belt.

The Daban Fault divides the CAB from the NAOB in its northern side (Fig. 1b); the former consists of Neoproterozoic Altyn Group amphibolite-facies felsic gneisses, marbles and amphibolites (Wang et al., 2013; Yu et al., 2013), and Mesproterozoic to Neoproterozoic Jinyanshan Group meta-sedimentary and meta-volcanic rocks (Zhang et al., 2014). Meanwhile, the inherited zircons from Altyn Group reveal the existence of Paleoproterozoic to Mesproterozoic crystalline basement in the CAB (Wang et al., 2013).

The SAOB is situated to the south of the CAB and is restricted to the NE–SW striking Altyn Tagh Fault. The presence of ultra-high pressure (UHP) eclogite (Liu et al., 2007), high pressure granulite (Liu et al., 2009) and various Ordvician magmatic rocks (Cao et al., 2010) indicate the SAOB is a typical collision orogenic belt (Zhang et al., 2015).

2.2. Sample descriptions

For the rebuilding of the evolution history of NAOB, samples were collected from the Abei Pluton, the 4337 Highland Pluton and the Kaladawan Pluton, which occur from north to south in the NAOB (Fig. 1c).

The Abei Pluton exposed over an area of >20 km^2 occurs at the intersection of the Northern Altun fault and its subordinate fault. The pluton comprises monzogranite (514 Ma, seen in the Section 4.1), biotite monzogranite and porphyritic granite. The biotite monzogranite and porphyritic granite (410–400 Ma, Meng et al., 2016) intruded the Cambrian volcanic-sedimentary rocks and in fault contact with the monzogranite (Fig. 1c). The different crystallization ages between these rocks imply they formed different settings and the monzogranite is the main study object in our paper. The monzogranite (Fig. 2a) is dominated by a fine- to medium-grained assemblage of K-feldspar (35–45%), plagioclase (25–30%), quartz (20–25%), biotite (<5%) and accessory minerals. Some quartzs form tiny grains due to dynamic recrystallization, others are undolose extinction (Fig. 3a).

The 4337 Highland Pluton is a homogeneous granodiorite intrusion of 50 km^2 in area, located in the northwest of the Kaladawan area. The intrusion is ~10 km long and is east–west trending (Fig. 1c); it is overlain by Quaternary sediments in the south and intruded Cambrian volcanic-sedimentary rocks in the north (Fig. 2b). This pluton is medium-grained and has a ductile–brittle gneissic structure (Fig. 2c) with a mineral assemblage of quartz (15–20%), K-feldspar (25–30%), plagioclase (35–45%), amphibole (10–15%) and minor biotite. Titanite, apatite, epidote and zircon generally occur as accessory minerals. The amphibole is typically aligned to form gneissic structure with the K-feldspar fragments and undolose extinction quartzs (Fig. 3b).

The Kaladawan granitic pluton, located on the southern margin of the NAOB, is ~15 km long and 2–3 km wide and lies along in the north of the volcanic magmatic arc represented by Ordovician volcanic–sedimentary rocks (Fig. 1c). It intrudes Cambrian volcanic-sediments (Fig. 2d) and consists mainly of quartz diorite, monzogranite and syenogranite (Fig. 2e and f). No sharp contacts between these rocks were observed in the field. The quartz diorite is medium-grained and consists of quartz (5–10%), plagioclase ($An_{30–40}$, 50–55%), amphibole (20–25%), biotite (5–10%, mainly altered to chlorite) and minor amounts of apatite, zircon and Fe-Ti oxides. The plagioclase is mainly andesine with zonal texture (Fig. 3c). The medium- to coarse- grained monzogranite is brown-red in color and comprises quartz (20–30%), K-feldspar (35–45%), plagioclase ($An_{15–25}$, 25–30%) and accessory apatite, zircon, epidote, titanite, and Fe–Ti oxides. The plagioclase is albite-andesine with multiple twins and the K-fledspar is altered to clay minerals (Fig. 3d). The fine-grained syenogranite contains quartz

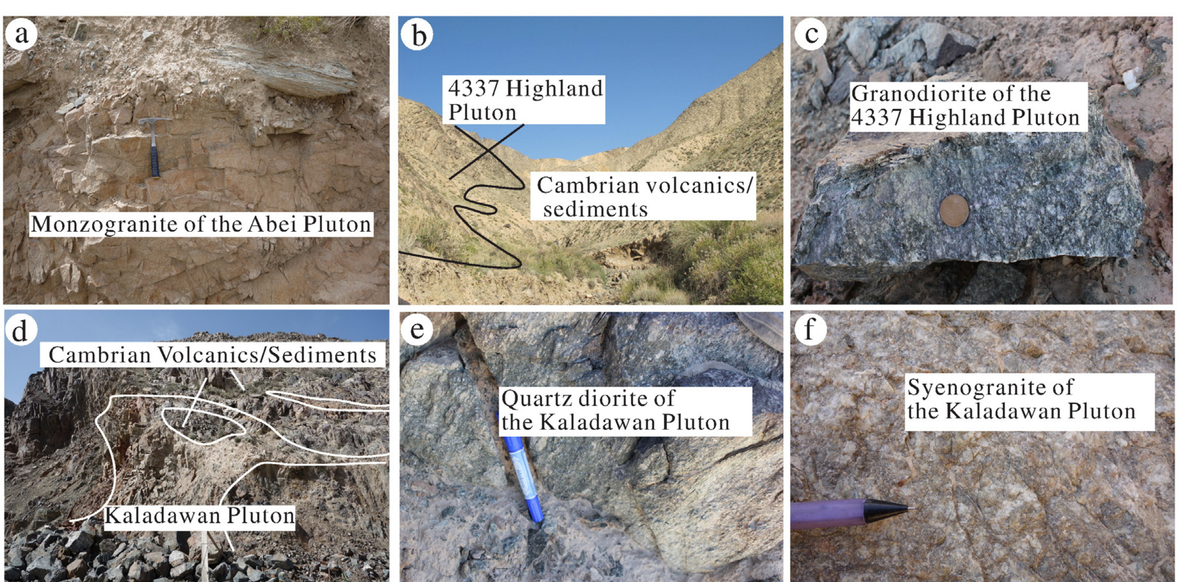

Fig. 2. Field photographs of early Paleozoic granitoid plutons in the NAOB, showing the compositions and contact relationships. (a) Monzogranite of the Abei Pluton; (b) intrusive contact between the 4337 Highland Pluton and Cambrian volcanic-sedimentary rocks; (c) intensely foliated granodiorite of the 4337 Highland Pluton; (d) intrusive contact between the Kaladawan Pluton and Cambrian volcanic-sedimentary rocks; (e) and (f) quartz diorite and syenogranite of the Kaladawan Pluton, respectively.

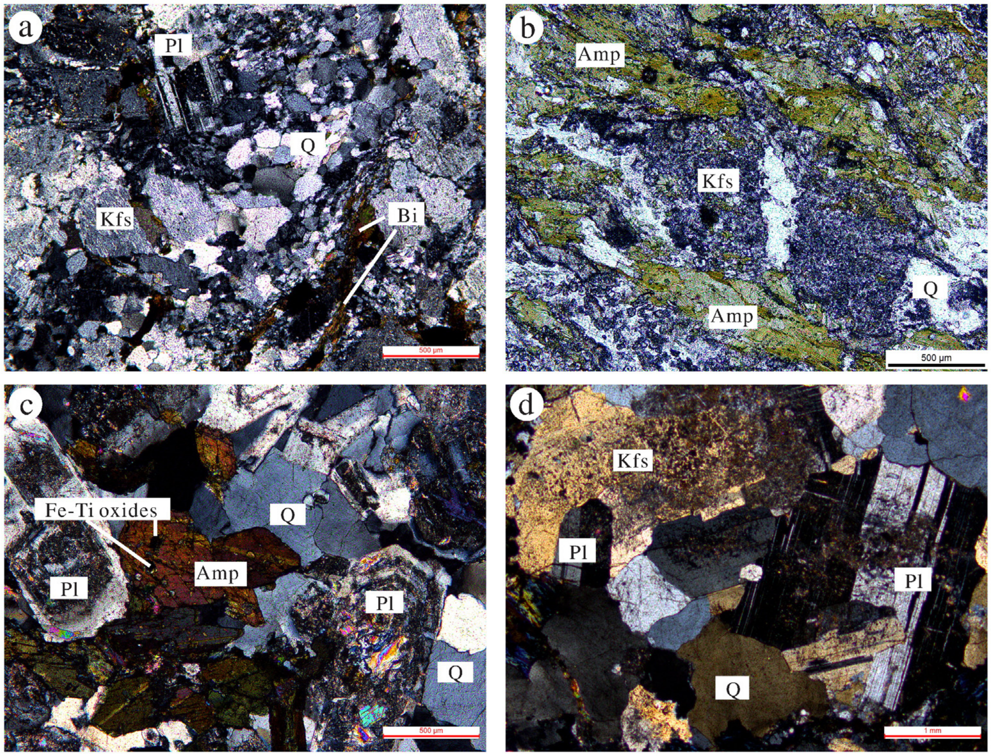

Fig. 3. Microphotographs of representative samples from Abei, 4337 Highland and Kaladawan Plutons in the NAOB. (a) Abei monzogranite (07A001-3, cross-polarized light); (b) 4337 Highland granodiorite (10H262-2, plane-polarized light); (c) Kaladawan quartz diorite (14K908-3, cross-polarized light); (d) Kaladawan monzogranite (12K429-3, cross-polarized light). Mineral abbreviations: Q = quartz, Kfs = K-feldspar, Pl = plagioclase, Bi = biotite, Amp = amphibole.

(25–30%), K-feldspar (50–60%), plagioclase (15–25%), biotite (5–10%), and accessory zircon, apatite, and epidote.

3. Analytical methods

3.1. Zircon U-Pb geochronology

Four representative fresh samples were chosen for SHRIMP zircon U–Pb analysis. Zircons were separated using conventional crushing and sieving, followed by standard magnetic and heavy-liquid separation techniques. They were then handpicked by a binocular microscope, mounted in epoxy and polished to expose the cores of the grains for cathodeluminescence (CL) imaging and isotopic analysis. The zircons were imaged under CL at the Institute of Geology and Geophysics, Chinese Academy of Sciences, Beijing, China. Zircon U–Pb analysis was conducted by SHRIMP II at Curtin University in Perth, Australia and the data were collected remotely at the Beijing SHRIMP Center, Institute of Geology, Chinese Academy of Geological Sciences, Beijing using the SHRIMP Remote Operation System. Details of the analyses and settings can be found in Song et al. (2002). The primary ion current was 4–6 nA and the spot diameter was 25–30 μm. The TEM (417 Ma) and SL13 (572 Ma, U = 238 ppm) were used as an external standard for age correction and U, Th contents, respectively. The analytical data are presented in Table 1. Errors for individual analyses were given at the 1σ level, and deviations for pooled analyses were given at the 95% confidence level. Concordia diagrams and weighted mean ages were produced using the programs ISOPLOT Version 3.0 (Ludwig, 2003).

3.2. In situ zircon Lu-Hf isotopic analyses

In situ zircon Lu-Hf isotopic analyses were carried out at the State Key Laboratory of Geological Process and Minerals Resources, China University of Geosciences, Wuhan, China. A Nu Plasma II MC-ICP-MS was used for determination for the Lu-Hf isotopes. The analyses were conducted using a spot size of 50 μm, a 10 Hz repetition rate and a laser power of 40 mJ/pulse. ^{179}Hf/^{177}Hf = 0.7325 (Chu et al., 2002) and $\beta_{Yb} = 0.8725 \times \beta_{Hf}$ (Xu et al., 2004) were used for the instrumental mass bias correction of Hf isotopes and instrumental mass bias coefficient (β) calculation of Yb isotopes. The ^{176}Yb/^{172}Yb = 0.5886 and ^{176}Lu/^{175}Lu = 0.02655 were determined to correct the isobaric interferences of ^{176}Lu and ^{176}Yb on ^{176}Hf (Chu et al., 2002). The weighted mean ^{176}Hf/^{177}Hf ratio of 0.282301 ± 0.000017 from the standard zircon 91,500 was similar to the ratio of 0.282307 ± 0.000031 reported by the previous reference (Wu et al., 2006).

The values of $\varepsilon_{Hf}(t)$, T_{DM}, T^2_{DM}, and $(^{176}Lu/^{177}Hf)_i$ were calculated by the equations as following:

$$\varepsilon_{Hf}(t) = \left(\left(\left(^{176}Hf/^{177}Hf\right)_S - \left(^{176}Lu/^{177}Hf\right)_S \times (e^{\lambda t}-1)\right) \Big/ \left(\left(^{176}Hf/^{177}Hf\right)_{CHUR,0} - \left(^{176}Lu/^{177}Hf\right)_{CHUR} \times (e^{\lambda t}-1)\right) - 1\right) \times 1000$$

$$T_{DM} = 1/\lambda \times \left(1 + \left(\left(^{176}Hf/^{177}Hf\right)_S - \left(^{176}Hf/^{177}Hf\right)_{DM}\right) \Big/ \left(\left(^{176}Lu/^{177}Hf\right)_S - \left(^{176}Lu/^{177}Hf\right)_{DM}\right)\right)$$

$$T_{DM}{}^2 = T_{DM} - (T_{DM} - t)\left(\left(\left(\left(^{176}Lu/^{177}Hf\right)_{LC} / \left(^{176}Lu/^{177}Hf\right)_{CHUR} - 1\right) - \left(\left(^{176}Lu/^{177}Hf\right)_S / \left(^{176}Lu/^{177}Hf\right)_{CHUR} - 1\right)\right) \Big/ \left(\left(\left(^{176}Lu/^{177}Hf\right)_{LC} / \left(^{176}Lu/^{177}Hf\right)_{CHUR} - 1\right) - \left(\left(^{176}Lu/^{177}Hf\right)_{DM} / \left(^{176}Lu/^{177}Hf\right)_{CHUR} - 1\right)\right)\right)$$

$$\left(^{176}Lu/^{177}Hf\right)_i = \left(^{176}Hf/^{177}Hf\right)_S - \left(^{176}Lu/^{177}Hf\right)_S \times (e^{\lambda t} - 1)$$

Table 1
SHRIMP U-Pb dating data of zircons from Abei Pluton, 4337 Highland Pluton and Kaladawan Pluton in North Altun orogenic belt, respectively.

Sample	Content (ppm)			Th/U	Age (Ma, 1σ)	Ratios			
	U	Th	$^{206}Pb^*$		$^{206}Pb/^{238}U$	$^{207}Pb^*/^{235}U$	1σ	$^{206}Pb^*/^{238}U$	1σ
Abei Pluton (monzogranite)									
07A001-3.1	400	193	29.4	0.48	530.4 ± 9.5	0.672	0.028	0.0856	0.017
07A001-3.2	573	348	39.7	0.61	500.7 ± 9.1	0.643	0.022	0.0807	0.017
07A001-3.3	594	538	42.1	0.91	511.4 ± 9.8	0.639	0.025	0.0823	0.017
07A001-3.4	1083	1184	78.0	1.09	520.0 ± 10	0.663	0.022	0.0837	0.017
07A001-3.5	662	574	47.7	0.87	520.1 ± 10	0.666	0.021	0.0839	0.017
07A001-3.6	308	230	22.2	0.75	517.8 ± 9.9	0.687	0.026	0.0838	0.018
07A001-3.7	199	103	14.0	0.52	507.6 ± 9.7	0.650	0.043	0.0819	0.018
07A001-3.8	350	182	25.2	0.52	519.3 ± 9.5	0.649	0.029	0.0836	0.017
07A001-3.9	417	112	29.5	0.27	510.5 ± 8.9	0.689	0.024	0.0824	0.017
07A001-3.10	426	250	30.1	0.59	509.8 ± 9.3	0.666	0.023	0.0830	0.017
07A001-3.11	254	149	18.3	0.59	518.3 ± 9.9	0.650	0.034	0.0825	0.018
07A001-3.12	577	384	41.1	0.67	514.3 ± 9.4	0.670	0.027	0.0827	0.017
Weighted mean of 12 points									
4337 Highland Pluton (granodiorite)									
10H262-2.1	606	200	42.8	0.33	498.8 ± 9.7	0.646	0.044	0.0805	0.020
10H262-2.2	240	123	16.6	0.51	496.8 ± 9.3	0.657	0.050	0.0803	0.019
10H262-2.3	407	146	27.8	0.36	490.2 ± 8.7	0.635	0.025	0.0791	0.018
10H262-2.4	915	370	63.4	0.40	498.9 ± 8.6	0.667	0.021	0.0807	0.018
10H262-2.5	336	192	27.4	0.57	494.5 ± 9.8	0.783	0.064	0.0809	0.018
10H262-2.6	323	152	21.7	0.47	481.0 ± 8.9	0.647	0.027	0.0778	0.019
10H262-2.7	306	130	21.3	0.42	497.0 ± 9.1	0.692	0.027	0.0807	0.019
10H262-2.8	1103	507	75.3	0.46	491.6 ± 8.4	0.641	0.021	0.0794	0.018
10H262-2.9	1234	552	87.0	0.45	500.6 ± 8.8	0.648	0.023	0.0808	0.018
10H262-2.10	307	131	20.9	0.43	487.8 ± 9.1	0.661	0.027	0.0790	0.019
10H262-2.11	275	101	19.5	0.37	505.5 ± 9.5	0.688	0.054	0.0819	0.019
10H262-2.12	747	155	72.3	0.21	675.0 ± 12.0	1.13	0.025	0.112	0.018
Weighted mean of 11 points									
Kaladawan Pluton (quartz diorite)									
14K908-3.1	736	388	49.1	0.53	482.6 ± 8.6	0.625	0.019	0.0774	0.017
14K908-3.2	393	201	26	0.51	477.9 ± 8.6	0.640	0.021	0.0768	0.017
14K908-3.3	758	298	50.3	0.39	479.8 ± 8.2	0.631	0.019	0.0772	0.017
14K908-3.4	897	598	59.4	0.67	479.6 ± 8.6	0.640	0.019	0.0769	0.017
14K908-3.5	974	802	64	0.82	474.4 ± 8.8	0.606	0.019	0.0763	0.017
14K908-3.6	456	234	30.2	0.51	477.7 ± 8.5	0.619	0.021	0.0770	0.017
14K908-3.7	1201	1234	81.5	1.03	489.9 ± 9.3	0.660	0.023	0.0786	0.017
14K908-3.8	759	469	50.4	0.62	480.8 ± 8.6	0.618	0.019	0.0773	0.017
14K908-3.9	920	698	60.6	0.76	476.2 ± 8.7	0.608	0.019	0.0766	0.017
14K908-3.10	675	532	46.7	0.79	497.3 ± 9.2	0.600	0.020	0.0804	0.017
14K908-3.11	781	415	51.1	0.53	473.3 ± 8.3	0.616	0.019	0.0760	0.017
14K908-3.12	721	318	47.4	0.44	475.6 ± 8.2	0.630	0.019	0.0763	0.017
14K908-3.13	491	252	31.6	0.51	466.9 ± 8.3	0.611	0.020	0.0748	0.017
14K908-3.14	1156	613	70.2	0.53	438.3 ± 7.7	0.506	0.019	0.0706	0.016
14K908-3.15	491	238	33.3	0.48	489.0 ± 8.7	0.603	0.021	0.0789	0.017
14K908-3.16	937	578	61.2	0.62	472.5 ± 8.4	0.601	0.019	0.0759	0.017
14K908-3.17	749	554	47.9	0.74	464.0 ± 8.5	0.607	0.019	0.0743	0.017
Weighted mean of 16 points									
Kaladawan Pluton (monzogranite)									
12K429-3.1	787	483	53	0.61	466.0 ± 8.8	0.641	0.075	0.0750	0.020
12K429-3.2	354	147	22.6	0.42	462.5 ± 8.9	0.594	0.029	0.0744	0.020
12K429-3.3	210	75	13.4	0.36	461.9 ± 9.5	0.591	0.040	0.0743	0.021
12K429-3.4	336	94	21.9	0.28	470.4 ± 9.2	0.603	0.039	0.0757	0.020
12K429-3.5	466	258	30	0.55	466.2 ± 8.8	0.587	0.028	0.0750	0.020
12K429-3.6	488	246	30.8	0.50	450.3 ± 8.6	0.589	0.063	0.0723	0.020
12K429-3.7	316	124	20	0.39	455.1 ± 8.9	0.532	0.044	0.0731	0.020
12K429-3.8	449	210	28.7	0.47	458.5 ± 8.7	0.564	0.041	0.0737	0.020
12K429-3.9	227	81	16.2	0.36	460 ± 12	0.52	0.280	0.0740	0.028
12K429-3.10	185	56	11	0.30	430.3 ± 9.1	0.533	0.046	0.0690	0.022
12K429-3.11	243	86	15.2	0.35	451.7 ± 9.2	0.544	0.059	0.0726	0.021
12K429-3.12	312	140	19.8	0.45	447.8 ± 9.3	0.615	0.098	0.0719	0.022
Weighted mean of 8 points									

where, $(^{176}Hf/^{177}Hf)_S$ and $(^{176}Lu/^{177}Hf)_S$ are test results of our samples, $(^{176}Lu/^{177}Hf)_{CHUR} = 0.0336$ and $(^{176}Hf/^{177}Hf)_{CHUR,0} = 0.282785$ (Bouvier et al., 2008), $(^{176}Hf/^{177}Hf)_{DM} = 0.282785$ and $(^{176}Lu/^{177}Hf)_{DM} = 0.0384$ (Griffin et al., 2000), $(^{176}Lu/^{177}Hf)_{LC} = 0.015$ (Griffin et al., 2002). A decay constant (λ) is adopted for ^{176}Lu of 1.865×10^{-11} year^{-1} (Scherer et al., 2001). Meanwhile, these values were calculated by using their magma crystallization ages (t) in every spots.

3.3. Whole-rock geochemical analysis

Twenty-one rock samples were selected for whole-rock major and trace element analyses. Major elements were analyzed on fused-glass disks by X-ray fluorescence spectrometry (XRF), except the FeO determined by the way of volumetric titration for which potassium dichromate (0.002319 mol/L) is used as the reagent. And trace elements, including rare earth elements (REEs), were determined by inductively coupled plasma mass spectrometry (ICP-MS). All the experiments were conducted at the National Research Center for Geoanalysis in Beijing, China. GBW07111 is used as the standard sample to correct the systematic error; its test and reference values are given in Table 3.The analytical uncertainties for major elements are within 1%, except for P_2O_5 (5%), and

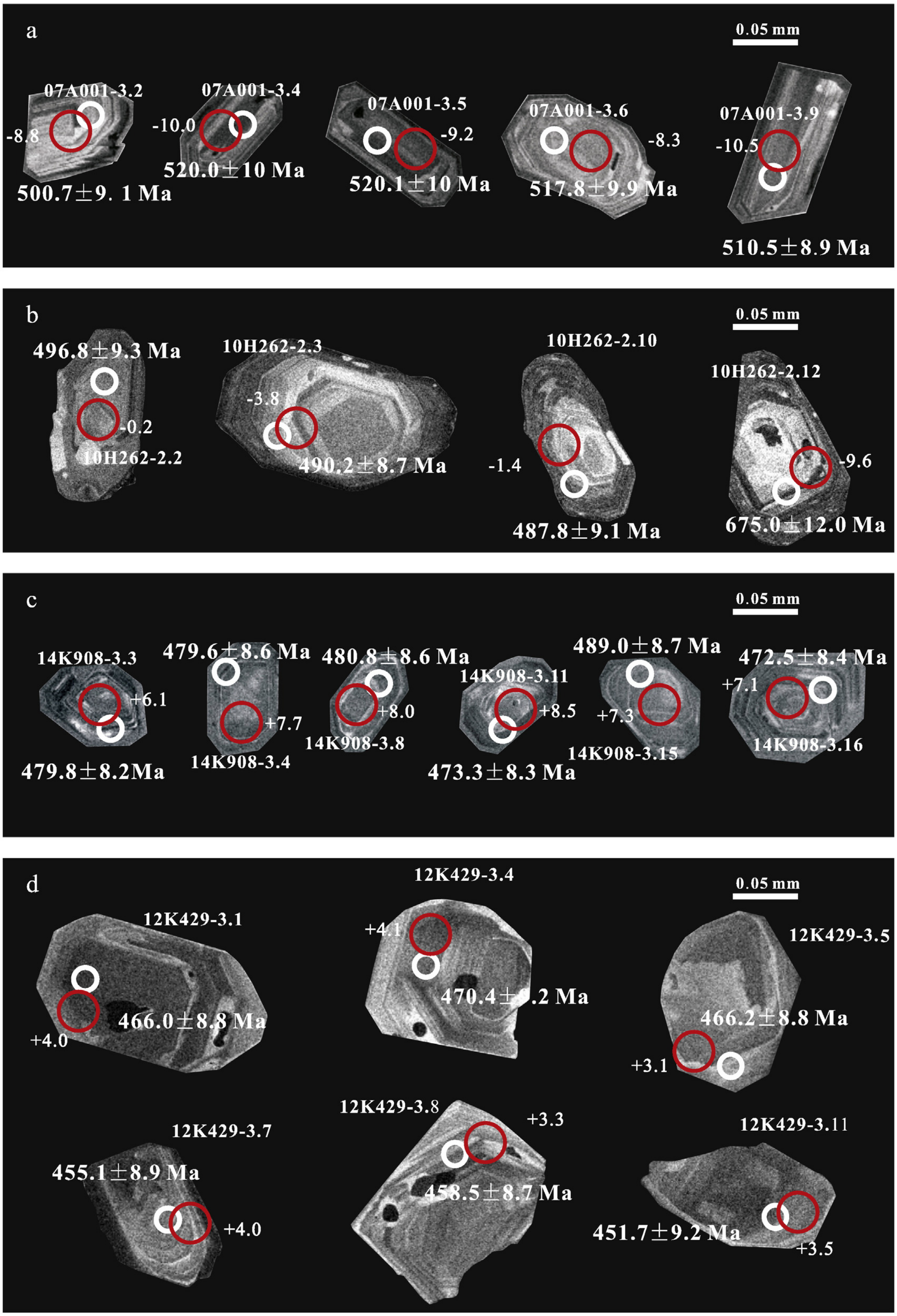

Fig. 4. Representative CL images of zircon grains showing spots for zircon SHRIMP U–Pb dating (white circles) and in situ zircon Lu-Hf isotopic analyses (red circles). (a) Abei monzogranite (07A001-3); (b) 4337 Highland granodiorite (10H262-2); (c) Kaladawan quartz diorite (14K908-3); (d) Kaladawan monzogranite (12K429-3). (For interpretation of the references to colour in this figure legend, the reader is referred to the online version of this chapter.)

are within 10% for most trace elements (including REEs). The detailed analytical procedures see the description of Zhang et al. (2009).

4. Results

4.1. Zircon U–Pb dating

Four samples were chosen for zircon U–Pb dating: monzogranite (07A001-3) from the Abei Pluton, granodiorite (10H262-2) from the 4337 Highland Pluton, and quartz diorite (14K908-3) and monzogranite (12K429-3) from the Kaladawan Pluton. The zircons from these samples are similar in crystal morphology and are characterized by transparent, euhedral crystals with lengths up to 150 μm. The CL images show oscillatory zoning and rare inherited cores (Fig. 4). The Th/U ratios are all >0.1, indicating a magmatic origin (Table 1). Twelve analyses from sample 07A001-3 were concordant and yielded a weighted mean age of 514.3 ± 5.6 Ma (Fig. 5a). A total of twelve spots from sample 10H262-2 were analyzed for dating, apart from spot 10H262-2.12 which represent the age of inherited core, yielding a concordant age of 494.4 ± 5.5 Ma (Fig. 5b). Of the seventeen analyses of sample 14K908-3, spot 14K908-3.14 had a younger discordant age because of the loss of Pb and was rejected; the remaining sixteen analyses yielded a weighted mean age of 477 ± 3.7 Ma (Fig. 5c). Twelve U-Pb isotopic analyses were carried out on sample 12K429-3. Except for four similar but discordant $^{206}Pb/^{238}U$ age (e.g. 12K429-3.1, 12K429-3.9, 12K429-3.10, 12K429-3.12), the remaining eight analyses yielded a weighted mean age of 459.5 ± 6.4 Ma which is emplacement age of monzogranite of Kaladawan Pluton (Fig. 5d).

4.2. Zircon Lu-Hf isotopic compositions

The samples dated were also chosen for the in situ zircon Lu-Hf isotopic analyses and all of the spots are located on or close to the site where the U-Pb dating was done (Fig. 4). The Lu-Hf isotopic data are listed in the Table 2 and plotted in Fig. 6.

The sixteen spots from sample 07A001-3 (Abei monzogranite) with the age of 514 Ma are analyzed, yielding initial $^{176}Hf/^{177}Hf$ values from 0.282140 to 0.282225, $\varepsilon_{Hf}(t)$ values from −8.3 to −11.4 and T^2_{DM} values from 2.0 to 2.2 Ga. The fifteen spots from sample 10H262-2 (4337 Highland granodiorite) with the age of 494 Ma display a wide range of initial $^{176}Hf/^{177}Hf$ values, from 0.282328 to 0.282479. Meanwhile, the $\varepsilon_{Hf}(t)$ values and T^2_{DM} values are range from −5.4 to +0.2 and from 1.4 to 1.7 Ga, respectively. The spot 10H262-2.12, however, exhibits the lower initial $^{176}Hf/^{177}Hf$ values and $\varepsilon_{Hf}(t)$ because it's an inherited zircon. The eighteen spots from sample 14K908-3 (Kaladawan quartz diorite) with the age of 477 Ma are characterized by high initial $^{176}Hf/^{177}Hf$ values (0.282638 to 0.282728) and positive $\varepsilon_{Hf}(t)$ values (+5.4 to +8.5) with the young T^2_{DM} values (0.8 to 1.0 Ga). Fifteen spots from the sample 12K429-3 (Kaladawan monzogranite) with the age of 459 Ma give initial $^{176}Hf/^{177}Hf$ from 0.282528 to 0.282611, $\varepsilon_{Hf}(t)$ values from +1.1 to +4.1 and T^2_{DM} values from 1.1 to 1.3 Ga.

4.3. Major and trace elements

The results of twenty-one samples are listed on the Table 3. The low LOI (lost on ignition) of these samples show they are less-alteration and fresh except the 12A439-1 (LOI = 2.78) and 12A480-3 (LOI = 3.66) which are lower Na_2O (Table 3). Fortunately, other elements (e.g. Rb,

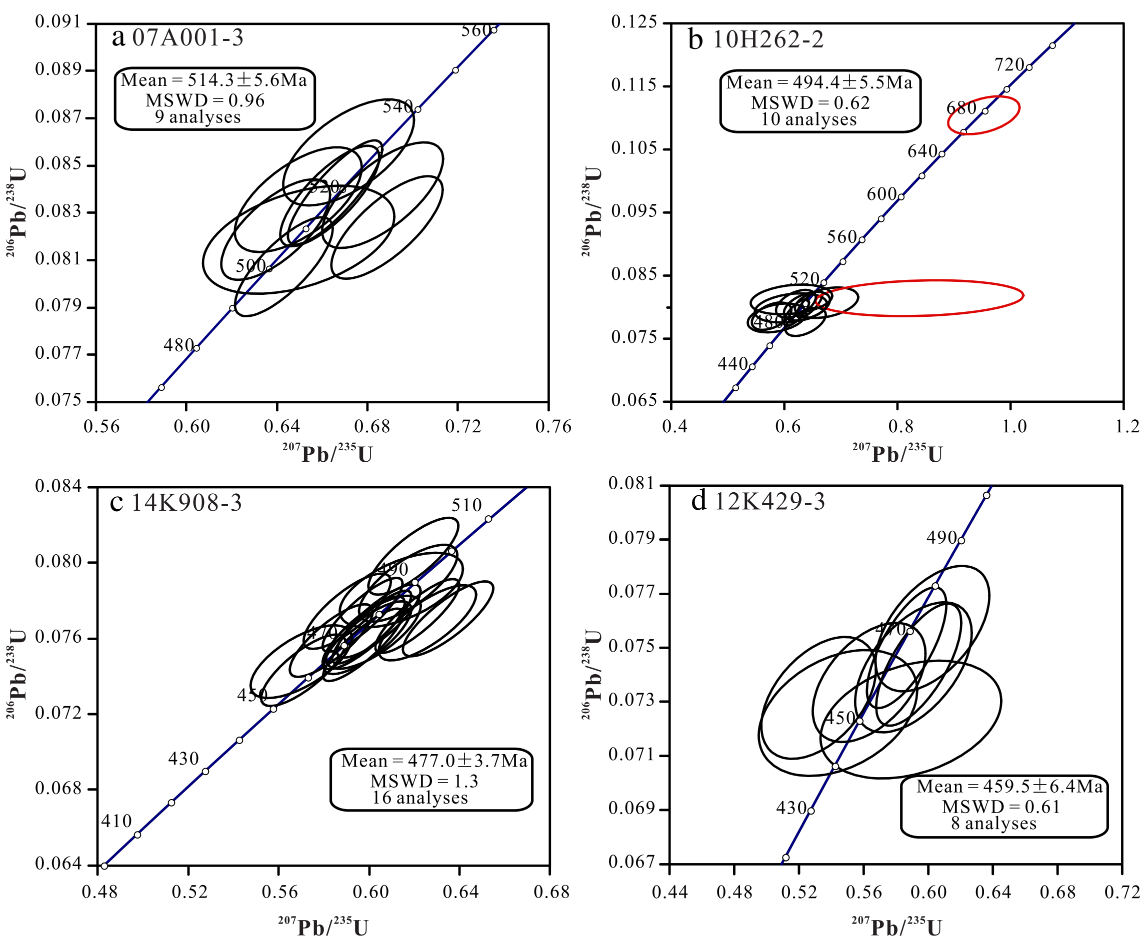

Fig. 5. U–Pb concordia diagrams for (a) Abei monzogranite (07A001-3); (b) 4337 Highland granodiorite (10H262-2); (c) Kaladawan quartz diorite (14K908-3); (d) Kaladawan monzogranite (12K429-3).

Table 2
In situ ziron Lu-Hf isotopic data from Abei Pluton, 4337 Highland Pluton and Kaladawan Pluton in North Altun orogenic belt, respectively.

Sample	$^{176}Hf/^{177}Hf$	Error	$^{176}Yb/^{177}Hf$	Error	$^{176}Lu/^{177}Hf$	Error	$(^{176}Lu/^{177}Hf)_i$	Age	$\varepsilon_{Hf}(t)$	2σ	T_{DM}	2σ	T_{DM}^2	2σ
Abei Pluton (monzogranite)														
07A001-3.1	0.282213	0.000014	0.030543	0.000112	0.001238	0.000004	0.282200	530	−8.9	0.5	1475	20	2030	32
07A001-3.2	0.282232	0.000014	0.034249	0.000597	0.001332	0.000019	0.282219	501	−8.8	0.5	1451	19	2006	31
07A001-3.3	0.282205	0.000015	0.043772	0.000135	0.001708	0.000005	0.282189	511	−9.7	0.5	1504	21	2068	33
07A001-3.4	0.282189	0.000014	0.035901	0.000661	0.001399	0.000024	0.282175	520	−10.0	0.5	1515	19	2093	31
07A001-3.5	0.282216	0.000014	0.049952	0.000479	0.001947	0.000017	0.282197	520	−9.2	0.5	1499	20	2045	31
07A001-3.6	0.282237	0.000015	0.035655	0.000190	0.001439	0.000008	0.282223	518	−8.3	0.5	1448	21	1987	33
07A001-3.7	0.282235	0.000014	0.025804	0.000198	0.001056	0.000008	0.282225	508	−8.5	0.5	1437	19	1990	30
07A001-3.8	0.282216	0.000013	0.031525	0.000117	0.001264	0.000005	0.282204	519	−9.0	0.5	1471	18	2030	29
07A001-3.9	0.282183	0.000012	0.046977	0.000141	0.001826	0.000053	0.282165	511	−10.5	0.4	1540	17	2120	27
07A001-3.10	0.282200	0.000016	0.029690	0.000514	0.001193	0.000019	0.282189	510	−9.7	0.6	1490	22	2069	35
07A001-3.11	0.282160	0.000013	0.035374	0.000640	0.001373	0.000024	0.282146	518	−11.1	0.4	1555	18	2158	28
07A001-3.12	0.282189	0.000014	0.029088	0.000309	0.001167	0.000001	0.282178	514	−10.0	0.5	1505	19	2091	31
07A001-3.13	0.282151	0.000013	0.028195	0.000281	0.001135	0.000011	0.282140	514	−11.4	0.5	1557	18	2174	28
07A001-3.14	0.282233	0.000015	0.034125	0.000125	0.001433	0.000006	0.282219	514	−8.6	0.5	1454	21	1999	33
07A001-3.15	0.282220	0.000012	0.020770	0.000019	0.000847	0.000001	0.282212	514	−8.8	0.4	1449	17	2014	28
07A001-3.16	0.282210	0.000012	0.030115	0.000248	0.001208	0.000010	0.282199	514	−9.3	0.4	1477	17	2044	27
4337 Highland Pluton (granodiorite)														
10H262-2.1	0.282389	0.000012	0.011325	0.000066	0.000467	0.000003	0.282385	499	−3.0	0.4	1202	17	1639	27
10H262-2.2	0.282470	0.000014	0.009174	0.000115	0.000390	0.000005	0.282467	497	−0.2	0.5	1087	19	1456	30
10H262-2.3	0.282374	0.000015	0.009191	0.000111	0.000413	0.000005	0.282370	490	−3.8	0.5	1221	20	1677	33
10H262-2.4	0.282479	0.000014	0.014390	0.000187	0.000600	0.000008	0.282473	499	0.1	0.5	1082	19	1441	31
10H262-2.5	0.282402	0.000015	0.019300	0.000260	0.000718	0.000010	0.282395	495	−2.8	0.5	1193	21	1618	34
10H262-2.6	0.282337	0.000014	0.024975	0.000390	0.000978	0.000015	0.282328	481	−5.4	0.5	1291	19	1777	31
10H262-2.7	0.282379	0.000018	0.011772	0.000081	0.000487	0.000004	0.282374	497	−3.5	0.6	1217	24	1664	39
10H262-2.8	0.282446	0.000013	0.016492	0.000417	0.000640	0.000014	0.282440	492	−1.2	0.5	1129	18	1520	30
10H262-2.9	0.282451	0.000014	0.018864	0.000154	0.000154	0.000006	0.282449	501	−0.7	0.5	1108	19	1493	31
10H262-2.10	0.282442	0.000014	0.011299	0.000012	0.000468	0.000000	0.282438	488	−1.4	0.5	1129	19	1527	30
10H262-2.11	0.282411	0.000014	0.016017	0.000052	0.000668	0.000002	0.282405	506	−2.2	0.5	1178	19	1589	31
10H262-2.12	0.282099	0.000014	0.022206	0.000141	0.000833	0.000004	0.282088	675	−9.6	0.5	1617	20	2188	32
10H262-2.13	0.282471	0.000015	0.014110	0.000023	0.000586	0.000001	0.282466	494	−0.3	0.5	1092	20	1460	33
10H262-2.14	0.282489	0.000016	0.030900	0.000518	0.001109	0.000016	0.282479	494	0.2	0.6	1082	23	1431	36
10H262-2.15	0.282480	0.000015	0.021209	0.000115	0.000850	0.000004	0.282472	494	−0.1	0.5	1088	21	1447	33
10H262-2.16	0.282466	0.000013	0.016902	0.000100	0.000709	0.000005	0.282460	494	−0.5	0.5	1102	19	1474	30
Kaladawan Pluton (quartz diorite)														
14K908-3.1	0.282714	0.000017	0.045942	0.000196	0.001854	0.000007	0.282697	483	7.7	0.6	780	25	946	38
14K908-3.2	0.282710	0.000016	0.058828	0.001430	0.002357	0.000054	0.282688	478	7.2	0.5	797	23	970	35
14K908-3.3	0.282670	0.000014	0.039258	0.000236	0.001596	0.000009	0.282656	480	6.1	0.5	837	21	1042	32
14K908-3.4	0.282724	0.000019	0.065832	0.000229	0.002614	0.000010	0.282701	480	7.7	0.7	781	28	941	43
14K908-3.5	0.282665	0.000020	0.075987	0.000675	0.002995	0.000024	0.282638	474	5.4	0.7	878	30	1085	45
14K908-3.6	0.282705	0.000017	0.042246	0.000193	0.001706	0.000007	0.282689	478	7.3	0.6	790	24	968	38
14K908-3.7	0.282736	0.000020	0.104893	0.001630	0.004087	0.000061	0.282698	490	7.9	0.7	797	31	940	45
14K908-3.8	0.282731	0.000016	0.066745	0.000339	0.002643	0.000013	0.282707	481	8.0	0.6	772	24	925	36
14K908-3.9	0.282711	0.000017	0.039121	0.000274	0.001612	0.000011	0.282697	476	7.5	0.6	779	24	952	37
14K908-3.10	0.282735	0.000019	0.057862	0.000475	0.002329	0.000017	0.282713	497	8.5	0.7	760	28	902	43
14K908-3.11	0.282742	0.000018	0.039747	0.000072	0.001616	0.000003	0.282728	473	8.5	0.6	735	26	884	41
14K908-3.12	0.282708	0.000018	0.045193	0.000150	0.001832	0.000006	0.282692	476	7.3	0.6	787	26	963	41
14K908-3.13	0.282689	0.000022	0.038256	0.000236	0.001569	0.000010	0.282675	467	6.5	0.8	810	32	1006	50
14K908-3.14	0.282692	0.000013	0.025083	0.000168	0.001086	0.000007	0.282683	438	6.2	0.5	795	19	1008	30
14K908-3.15	0.282699	0.000018	0.046361	0.000155	0.001900	0.000005	0.282682	489	7.3	0.6	802	25	977	39
14K908-3.16	0.282707	0.000017	0.051849	0.000271	0.002076	0.000010	0.282689	473	7.1	0.6	795	25	972	39
14K908-3.17	0.282741	0.000024	0.058028	0.000854	0.002325	0.000033	0.282721	464	8.1	0.8	751	35	906	53
14K908-3.18	0.282725	0.000018	0.029194	0.000134	0.001176	0.000005	0.282715	477	8.2	0.6	750	25	911	39
Kaladawan Pluton (monzogranite)														
12K429-3.1	0.282625	0.000018	0.058590	0.000426	0.002243	0.000016	0.282606	466	4.0	0.6	918	26	1164	40
12K429-3.2	0.282616	0.000019	0.073377	0.000338	0.002756	0.000011	0.282592	463	3.5	0.7	944	27	1196	42
12K429-3.3	0.282567	0.000018	0.027152	0.000202	0.001082	0.000008	0.282558	462	2.3	0.6	971	25	1274	40
12K429-3.4	0.282608	0.000014	0.013005	0.000119	0.000513	0.000005	0.282604	470	4.1	0.5	900	19	1166	32
12K429-3.5	0.282598	0.000017	0.053057	0.000131	0.002024	0.000006	0.282580	466	3.1	0.6	952	24	1221	38
12K429-3.6	0.282541	0.000018	0.027383	0.000308	0.001090	0.000012	0.282532	450	1.1	0.6	1008	25	1339	41
12K429-3.7	0.282622	0.000015	0.031119	0.000069	0.001198	0.000003	0.282611	455	4.0	0.5	897	21	1158	34
12K429-3.8	0.282597	0.000016	0.022679	0.000133	0.000886	0.000005	0.282590	459	3.3	0.6	924	22	1204	36
12K429-3.9	0.282605	0.000017	0.067193	0.000072	0.002523	0.000003	0.282584	460	3.1	0.6	954	24	1217	38
12K429-3.10	0.282593	0.000016	0.014007	0.000037	0.000558	0.000001	0.282589	430	2.6	0.6	922	23	1225	37
12K429-3.11	0.282608	0.000016	0.029116	0.000046	0.001121	0.000002	0.282598	452	3.5	0.6	915	23	1190	36
12K429-3.12	0.282596	0.000018	0.025520	0.000118	0.000994	0.000004	0.282587	448	3.0	0.6	929	26	1217	41
12K429-3.13	0.282557	0.000020	0.092795	0.000312	0.003370	0.000009	0.282528	459	1.1	0.7	1049	30	1343	46
12K429-3.14	0.282564	0.000019	0.031279	0.000164	0.001198	0.000006	0.282553	459	2.0	0.7	979	26	1286	42
12K429-3.15	0.282543	0.000017	0.033299	0.000151	0.001279	0.000005	0.282532	459	1.3	0.6	1011	24	1334	39

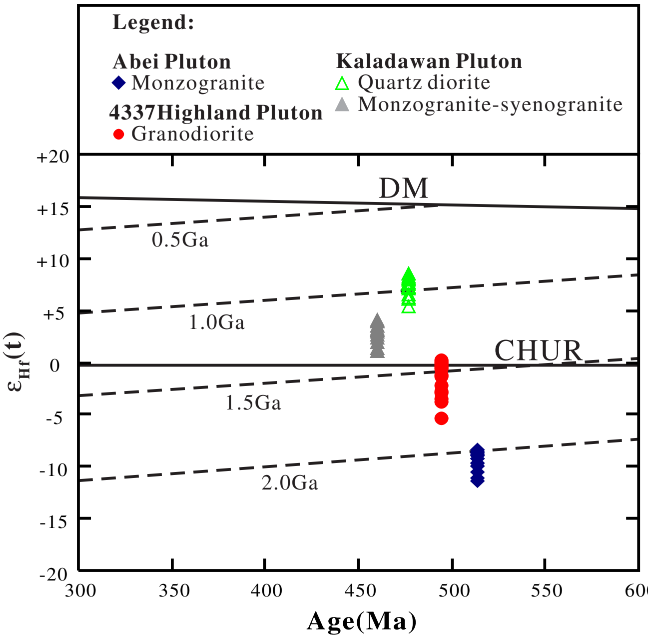

Fig. 6. Diagram of εHf(t) versus U-Pb ages in zircons for each sample analyzed (after Yang et al., 2015). Abbreviation: CHUR = chondritic uniform reservoir; DM = depleted mantle.

Sr, Ba) are unaffected because they are similar in all of six samples. The major elements are renormalized to let their sum to 100% after deduction of LOI (Table 3).

4.3.1. Abei Pluton

Six representative monzogranite samples of the Abei pluton were analyzed for whole-rock major and trace element compositions (Table 3). All samples are characterized by high SiO_2 (69.7–74.3%), Al_2O_3 (13.0–15.6%), K_2O (3.64–5.31%), medium Fe_2O_3 (2.08–3.60%), and low FeO (0.24–1.42%), MgO (0.41–1.36%), plotted in or near the granite field on the SiO_2 versus $Na_2O + K_2O$ diagram (Fig. 7a). The A/CNK ($[Al_2O_3 / (CaO + K_2O + Na_2O)]_{molar}$) ratios of samples are 1.08–1.61 (Table 3), indicating they are peraluminous (Fig. 7b). They also display the high-K calc-alkaline in Fig. 7c and the FeO^{total}/MgO ratios plot the samples in the transition region between ferroan and magnesian (Fig. 7d). REE data have moderately fractionated patterns ($(La/Yb)_N$ = 4.43–15.6) with an obvious negative Eu anomaly (Eu/Eu* = 0.46–0.55) in the chondrite-normalized REE diagram (Fig. 8a). Meanwhile, they exhibit strongly positive Th, U, K anomalies and negative Sr, Eu, high field-strength elements (HFSEs, e.g. Nb, Ta, Ti) anomalies in the primitive mantle-normalized trace element diagram (Fig. 8b).

4.3.2. 4337 Highland Pluton

Five representative samples of the 4337 Highland Pluton were selected for analyses of whole-rock major and trace element compositions (Table 3). They contain high SiO_2 (62.7–70.1%), K_2O (2.88–4.68%), Na_2O (2.82–4.36%), medium Fe_2O_3 (1.25–2.41%), FeO (1.68–3.55%), MgO (1.18–2.56%), and low TiO_2 (0.33–0.61%), P_2O_5 (0.15–0.36%). They are plotted in the granodiorite field on the SiO_2 versus $Na_2O + K_2O$ diagram (Fig. 7a) and the high-K calc-alkaline field on the SiO_2 versus K_2O diagram (Fig. 7c), respectively. These samples are metaluminous with the A/CNK ratios of 0.83–0.98 (Fig. 7b). They have low Fe/Mg ratios and are magnesian (Fig. 7d), indicating they formed high oxygen fugacity environment (Frost and Frost, 2008). They have strongly fractionated REE patterns ($(La/Yb)_N$ = 19.7–26.4) with a weakly to no negative Eu anomaly (Eu/Eu* = 0.72–0.97) (Fig. 8c). The characteristic of lower HREEs, Yb, Y, and higher Sr, $(La/Yb)_N$ than other samples in Table 3 are similar to those of "adakite" (e.g. Wang et al., 2005, Fig. 8c–d). In the primitive mantle-normalized trace element diagram (Fig. 8d), they show variable enrichments in Ba, Th, Sr, and K, and depletion in Nb–Ta, P, and Ti.

4.3.3. Kaladawan Pluton

Four quartz diorite samples and six monzogranite–syenogranite samples from the Kaladawan Pluton were analyzed for whole-rock major and trace element compositions (Table 3). On the SiO_2 versus $K_2O + Na_2O$ diagram (Fig. 7a), the samples are plotted in the quartz diorite and granite fields, respectively, which are consistent with petrographic observations.

The quartz diorite samples have lower SiO_2 (58.1–61.2%), K_2O (1.47–1.83%), Na_2O (2.18–2.56%) and higher Fe_2O_3 (2.19–2.95%), FeO (3.63–5.05%), MgO (4.38–5.62%), Co (12.7–36.5 ppm), Ni (6.11–29.4 ppm) as well as $Mg^{\#}$ ($[100MgO / (MgO + FeO^{total})]_{molar}$, 57–64) than other samples examined in this study. They are plotted in the moderate-K calc-alkaline, metaluminous and magensian fields in Fig. 7b–d. In the chondrite-normalized REE (Fig. 8e) and primitive mantle-normalized trace element diagrams (Fig. 8f), they are characterized by weakly fractionated REE patterns ($(La/Yb)_N = 2.36$–6.38) with a weakly negative Eu anomaly (Eu/Eu* = 0.64–0.90) and depletion of P, Ti, Nb–Ta and Zr–Hf.

In contrast, the monzogranite–syenogranite samples have higher SiO_2 (73.3–77.3%), variable K_2O (0.47–5.16%), Na_2O (3.92–7.41%), but lower MgO (0.16–1.10%), $Mg^{\#}$ (14–46), Co (1.61–5.38 ppm), Ni (1.41–7.56 ppm) than the quartz diorite samples. They are plotted in the low to high-K calc-alkaline, metaluminous and magnesian to ferroan field in Fig. 7b–d. In the chondrite-normalized REE (Fig. 8g) and primitive mantle-normalized trace element diagrams (Fig. 8h), they show moderately fractionated REE patterns ($(La/Yb)_N$ = 7.19–12.1) with a strongly negative Eu anomaly (Eu/Eu* = 0.23–0.40), strongly positive Th, U anomalies and negative Ba, Sr, Eu, HFSEs (Nb, Ta, and Ti) anomalies.

5. Discussion

5.1. Magma sources and melting conditions

5.1.1. Abei Pluton

The Abei Pluton (514 Ma) is hornblende-bearing, peraluminous, high-K calc-alkaline monzogranite (Fig. 7) with high SiO_2, Al_2O_3, K_2O and low MgO, Cr, Co, Ni. Strongly positive Th, U and Pb anomalies, negative Nb, Ta, Ti, Sr, Eu anomalies and zircon $\varepsilon_{Hf}(t)$ values ($\varepsilon_{Hf}(t) = -8.3$ to -11.4) (Tables 2, 3; Figs. 6, 8a–b) imply that the pluton is mainly crustal origin. The Nb/Ta (9.94–13.6) and Nb/U (4.10–7.15) values of Abei Pluton also fall into the scope of crust (Green, 1995; Rudnick and Gao, 2003; Sylvester et al., 1997). Based on its old Hf second-stage model ages (T^2_{DM} = 2.0 to 2.2 Ga), we decipher the Paleoproterozoic protolith was reworked again during the early Paleozoic.

The negative Eu anomaly and low Sr/Y indicate that the magma was sourced from a shallow crustal level (low pressure), leaving a plagioclase-rich, garnet-free residue (Patiño Douce and Beard, 1995). Meanwhile, The magma temperature (>800 °C) calculated using the zircon saturation thermometer (Boehnke et al., 2013) is high enough for considerable dehydration melting of continental crust, implying that an influx of external fluid was not necessary to generate the magma (Miller et al., 2003). Although the Abei Pluton is peraluminous, the absence of Al-rich minerals (e.g., muscovite, garnet, and cordierite) and inherited zircons differentiates it from typical S-type granites (Chappell and Wyborn, 2012; Clemens, 2003). Moreover, Patiño Douce (1995) reported that dehydration melting of biotite gneiss and quartz amphibolite can produce peraluminous granitic melts with residual assembles of plagioclase ± pyroxene ± garnet depending on the pressure. Considering the existence of the Paleoproterozoic to Mesoproterozoic crystalline basement in the CAB,

Table 3
The geochemical compositions of Abei Pluton, 4337 Highland Pluton and Kaladawan Pluton in North Altun orogenic belt, respectively.

Sample Pluton	12A481-1 Abei	12A480-1	12A480-2	07A001-3	12A439-1	12A480-3	08H272-1 4337 Highland	10H262-2	08H272-2	10H139-1	10H140-2
Rock type	MG	MG	MG	MG	MG	MG	GD	GD	GD	GD	GD
Major element (wt.%)											
SiO_2	69.7	71.6	72.0	72.1	73.0	74.3	62.7	65.6	66.2	68.9	70.1
Al_2O_3	15.6	14.5	14.2	14.4	15.4	13.0	16.0	15.0	15.8	15.4	15.0
Fe_2O_3	3.30	2.08	3.60	2.48	2.27	3.12	2.41	1.65	1.98	1.66	1.25
FeO	0.47	1.42	0.29	0.44	0.49	0.24	3.55	3.02	2.27	1.68	1.88
CaO	3.42	2.15	3.33	2.33	2.03	3.34	5.23	4.33	4.43	3.18	2.94
MgO	0.63	1.36	0.64	0.41	0.78	0.81	2.56	1.71	1.74	1.18	1.24
K_2O	3.84	3.64	4.44	4.85	5.31	4.51	3.59	4.68	2.88	3.89	2.68
Na_2O	2.42	2.62	0.79	2.33	0.06	0.04	2.82	3.14	3.92	3.47	4.36
TiO_2	0.45	0.51	0.50	0.48	0.53	0.44	0.61	0.47	0.48	0.37	0.33
MnO	0.07	0.04	0.11	0.06	0.04	0.11	0.11	0.11	0.08	0.07	0.08
P_2O_5	0.13	0.07	0.08	0.10	0.08	0.07	0.36	0.27	0.26	0.17	0.15
LOI	1.61	1.55	1.68	0.32	2.78	3.66	0.64	1.23	0.61	1.35	0.78
K_2O+N_2O	6.26	6.26	5.23	7.19	5.38	4.55	6.41	7.82	6.80	7.35	7.05
A/NK	1.91	1.75	2.32	1.59	2.63	2.62	1.87	1.47	1.65	1.56	1.49
A/CNK	1.08	1.19	1.17	1.08	1.61	1.18	0.89	0.83	0.89	0.98	0.97
FeO^{total}	3.44	3.29	3.52	2.67	2.53	3.05	5.72	4.50	4.05	3.16	3.00
$Mg^{\#}$	0.25	0.43	0.25	0.22	0.36	0.32	0.45	0.41	0.44	0.40	0.43
Rare earth elements (ppm)											
La	26.6	39.8	48.4	39.2	31.1	55.3	68.4	60.3	68.1	54.8	35.9
Ce	56.9	86.2	102	79.9	62.1	115	122	111	107	105	66.6
Pr	6.89	8.75	10.4	9.23	7.03	11.9	13.5	12.7	12.2	10.1	6.75
Nd	28.6	32.2	38.5	34.1	26.3	43.2	49.4	45.1	41.4	36.4	23.7
Sm	6.05	5.61	7.03	7.12	4.59	7.28	8.76	8.12	7.09	6.03	3.74
Eu	0.96	0.87	1.14	1.01	0.67	1.00	2.10	1.88	2.02	1.46	0.77
Gd	6.06	4.85	5.80	5.97	4.24	5.46	7.63	6.00	5.73	4.45	2.82
Tb	1.04	0.70	0.97	1.10	0.69	0.82	0.97	0.77	1.04	0.64	0.39
Dy	6.28	3.84	5.31	6.64	4.24	4.53	5.40	4.45	4.58	3.06	1.93
Ho	1.32	0.76	1.05	1.38	0.84	0.84	0.97	0.85	0.76	0.59	0.35
Er	4.25	2.37	3.21	4.49	2.71	2.78	2.76	2.42	2.45	1.74	1.12
Tm	0.62	0.30	0.43	0.61	0.39	0.34	0.36	0.33	0.27	0.22	0.15
Yb	4.31	2.21	2.83	4.18	2.64	2.55	2.41	2.20	1.85	1.50	1.12
Y	38.5	20.2	30.5	42.0	25.0	25.3	25.5	23.4	20.6	17.70	11.7
Lu	0.67	0.33	0.41	0.63	0.41	0.40	0.35	0.32	0.28	0.23	0.19
Eu/Eu^*	0.48	0.51	0.55	0.47	0.46	0.48	0.79	0.82	0.97	0.86	0.72
$(La/Yb)_N$	4.43	12.9	12.3	6.73	8.45	15.6	20.4	19.7	26.4	26.2	23.0
Trace elements (ppm)											
Cr	18.1	36.9	20.8	32.4	22.8	22.1	15.9	15.0	131	9.31	13.2
Co	6.38	7.37	7.32	4.83	10.2	4.00	15.9	10.1	10.3	6.63	5.74
Ni	7.07	15.0	12.1	14.4	18.2	10.3	6.87	5.62	10.8	3.93	6.36
Cu	3.24	9.86	17.1	10.5	5.26	10.1	18.0	6.09	8.61	25.5	9.54
Zn	31.7	31.0	1939	119	349	535	82.1	65.8	72.2	68.4	81.2
Ga	19.1	16.5	17.3	18.3	18.7	15.8	17.6	18.0	18.9	20.0	20.3
Rb	145	143	180	179	194	177	96.2	207	91.8	195	159
Sr	70.1	56.1	25.7	49.5	16.5	27.8	620	528	697	509	353
Zr	156	207	214	216	235	186	224	158	197	176	154
Nb	19.6	12.6	12.9	17.6	13.6	11.6	16.3	20.6	16.1	16.5	22.9
Ba	500	277	269	450	211	290	1285	1128	1078	1252	826
Hf	5.01	5.97	5.96	6.41	6.35	4.92	5.87	4.37	5.12	4.47	3.83
Ta	1.74	1.06	1.13	1.77	1.00	0.93	0.94	1.39	1.27	1.52	1.21
Pb	13.4	21.0	724	407	16.1	1498	21.3	37.0	36.5	35.7	41.3
Th	13.1	16.2	18.1	19.9	14.0	18.9	22.0	33.2	22.0	20.2	19.2
U	2.74	3.01	2.60	3.66	2.48	2.83	2.80	6.44	3.46	3.44	3.32
Sr/Y	1.82	2.78	0.84	1.18	0.66	1.10	24.3	22.6	33.8	28.8	30.2
Normative mineral (wt.%)											
An	16.15	10.17	15.97	10.92	9.51	16.13	20.41	13.09	16.97	14.62	13.41
Ab	20.47	22.19	6.73	19.76	0.53	0.36	23.89	26.60	33.14	29.33	36.93
Or	22.73	21.53	26.27	28.70	31.44	26.68	21.22	27.65	17.02	22.97	15.87
Zircon saturation temperature (°C)											
T	807	863	868	852	937	858	780	737	779	796	781

Notes: The values of major elements A/NK = $[Al_2O_3/(Na_2O+K_2O)]_{molar}$; A/CNK = $[Al_2O_3/(Cao+Na_2O+K_2O)]_{molar}$; FeO^{total} = all Fe calculated as FeO; $Mg^{\#} = [100MgO/(MgO+FeO^{total})]_{molar}$. Abbreviation: LOI = lost on ignition; An = anorthite; Ab = albite; Or = orthoclase; MG = monzogranite; GD = granodiorite; QD = quartz diorite; SG = syenogranite. T (temperature) are calculated by the zircon saturation thermometer (Boehnke et al., 2013). GBW07111 is the standard sample, ① is its test values and ② is its reference values.

the Abei Pluton was likely interpreted to source from the recycle of old CAB continental crust (mainly igneous rocks) under low pressure and high temperature conditions. Although the characteristics of "hot granite" (e.g. Miller et al., 2003) it possess reveal that the underplating of mafic magma provides additional heat for dehydration melting of the continental crust, the homogeneous zircon Hf isotopic compositions (Table 2) exclude the possibility of mantle-derived material contribution to the magma source.

5.1.2. 4337 Highland Pluton

Geochemical data indicate that the 4337 Highland Pluton is potassium, calc-alkaline, metaluminous and has the features of "adakitic rocks" as

14K908-2	14K908-3	14K908-4	14K908-5	08K265-1	07K070-3	08K283-1	12K429-3	08K266-1	14K908-1	GBW07111	
Kaladawan										①	②
QD	QD	QD	QD	MG	MG	MG	MG	SG	SG	GD	
58.1	59.7	62.5	61.2	73.3	74.2	74.8	75.5	75.9	77.3	59.8	59.7
17.0	14.3	15.5	14.4	14.0	13.7	13.3	13.6	13.7	12.6	16.6	16.6
2.20	2.19	2.44	2.95	0.64	1.05	0.82	0.76	1.02	1.19	2.78	2.64
3.63	4.54	3.68	5.05	1.80	0.88	0.89	1.00	0.87	0.66	2.95	3.08
6.74	8.50	6.20	5.79	1.40	0.87	0.62	0.43	0.62	0.25	4.69	4.72
5.58	5.47	4.38	5.62	1.10	0.22	0.25	0.41	0.33	0.16	2.79	2.81
1.57	1.63	1.83	1.47	3.04	3.43	5.16	0.58	0.47	2.84	3.53	3.50
2.47	2.36	2.56	2.18	4.32	5.39	3.92	7.41	6.87	4.85	4.03	4.05
2.22	1.60	0.60	1.13	0.36	0.20	0.18	0.20	0.20	0.12	0.75	0.77
0.21	0.20	0.14	0.12	0.03	0.02	0.03	0.02	0.02	0.01	0.09	0.09
0.33	0.16	0.14	0.15	0.08	0.01	0.01	0.03	0.03	0.01	0.35	0.34
0.61	0.84	0.81	1.05	0.43	0.67	0.28	0.52	0.78	0.79	0.96	
4.04	4.00	4.39	3.65	7.36	8.82	9.08	7.99	7.34	7.69		
2.94	2.52	2.50	2.77	1.34	1.09	1.10	1.06	1.16	1.14		
0.94	0.67	0.89	0.91	1.08	0.96	1.01	1.00	1.06	1.09		
5.60	6.50	5.87	7.70	2.37	1.83	1.63	1.68	1.79	1.73		
0.64	0.60	0.57	0.57	0.46	0.18	0.22	0.31	0.25	0.14		
21.5	18.2	18.6	15.9	40.9	73.0	51.9	53.2	35.9	58.5	60.0	60.5
48.3	40.7	43.1	32.4	82.0	101	73.2	78.6	41.6	87.1	117	112
6.10	5.51	5.38	4.28	8.51	12.5	9.32	8.88	6.04	10.2	13.9	13.2
28.4	21.8	22.4	18.0	29.7	40.0	30.9	30.3	20.1	31.1	50.5	48.1
6.79	4.79	4.63	3.47	5.74	7.04	6.04	5.10	3.63	5.63	8.23	7.74
2.16	1.12	1.20	0.87	0.72	0.83	0.59	0.47	0.32	0.42	1.89	1.91
7.87	6.94	4.10	4.93	5.69	5.68	5.01	4.83	3.66	5.71	5.08	5.09
1.32	1.24	0.65	0.95	0.93	1.06	0.96	0.81	0.68	1.18	0.59	0.68
8.35	7.82	3.62	6.15	5.86	6.24	5.78	4.84	4.58	6.90	3.51	3.20
1.77	1.62	0.73	1.36	1.17	1.34	1.23	0.97	1.00	1.41	0.66	0.60
5.30	4.95	2.29	4.56	3.50	4.40	4.06	3.29	3.30	4.58	1.88	1.57
0.73	0.66	0.30	0.70	0.50	0.65	0.59	0.45	0.51	0.64	0.25	0.26
4.93	4.58	2.09	4.83	3.57	4.57	4.08	3.16	3.58	4.24	1.65	1.56
48.6	48.2	21.9	41.0	32.2	39.9	37.6	29.7	26.8	44.8	16.7	15.5
0.71	0.69	0.33	0.73	0.48	0.69	0.65	0.48	0.51	0.65	0.24	0.24
0.90	0.59	0.84	0.64	0.39	0.40	0.33	0.29	0.27	0.23		
3.13	2.85	6.38	2.36	8.22	11.5	9.12	12.1	7.19	9.90		
29.1	110	67.3	150	18.6	13.4	3.62	3.19	2.29	189	41.9	37.6
36.5	22.6	18.6	12.7	5.38	1.75	1.61	2.39	2.05	2.46	16.5	15.6
18.6	29.4	21.2	6.11	7.56	6.20	1.65	1.98	1.41	6.04	27.3	24.4
17.3	41.3	35.3	12.2	6.95	4.14	4.28	1.44	13.5	3.40	8.28	8.80
125	90.8	82.1	133	29.0	10.7	10.3	23.0	9.60	8.94	69.5	85.4
23.1	19.6	17.6	14.9	21.0	17.8	19.0	19.1	18.9	17.0	22.3	20.8
43.7	54.1	106	11.7	86.9	78.1	186	25.4	11.1	56.2	75.5	70.1
298	271	307	136	101	54.7	63.3	55.5	45.0	26.8	1220	1198
222	130	164	153	167	314	237	236	229	180	230	224
10.3	11.2	10.3	9.46	14.0	18.8	17.3	17.9	15.9	24.6	12.0	10.6
471	161	640	224	999	1030	1058	129	40.7	721	2221	1900
5.40	3.58	4.25	4.31	5.54	8.68	6.38	6.12	6.79	6.03	5.79	5.20
0.64	0.97	0.80	0.77	1.98	1.35	1.22	1.20	1.26	1.93	0.63	0.62
12.4	13.4	14.9	5.57	8.77	4.70	5.07	2.26	1.13	3.43	16.2	19.8
5.25	9.04	8.27	7.13	31.6	45.5	35.7	28.2	22.5	28.3	11.0	10.9
1.85	2.40	3.13	2.42	5.48	6.37	4.80	4.16	4.59	4.42	1.46	1.40
6.13	5.62	14.0	3.32	3.14	1.37	1.68	1.87	1.68	0.60		
17.03	29.74	22.49	5.43	6.41	2.99	3.03	1.96	2.87	1.19		
36.12	11.55	21.64	31.17	36.55	45.63	33.19	62.70	58.14	41.06		
9.26	6.09	16.74	2.76	17.98	20.25	30.49	3.40	2.76	16.79		
776	647	746	743	820	876	854	849	858	841		

seen in Section 4.3.2. In the Sr/Y–Y and $(La/Yb)_N$–$(Yb)_N$ diagrams (Fig. 9) the data of the granodiorites are closer to the scope of "adakitic rock" than other plutons, reflecting its formation is under higher pressure. In general, there are three genetic models for plutons under high pressure: (1) partial melting of a subducted oceanic slab (Defant and Drummond, 1990; Rapp and Watson, 1995; Rapp et al., 1999; Sen and Dunn, 1994); (2) partial melting of thickened or delaminated lower continental crust (Atherton and Petford, 1993; Barnes et al., 1996; Hou et al., 2004; Xu et al., 2002); and (3) fractional crystallization of basaltic magma (Castillo et al., 1999).

The model of fractional crystallization of basaltic magma should be firstly excluded because mafic intrusions related to the 4337 Highland

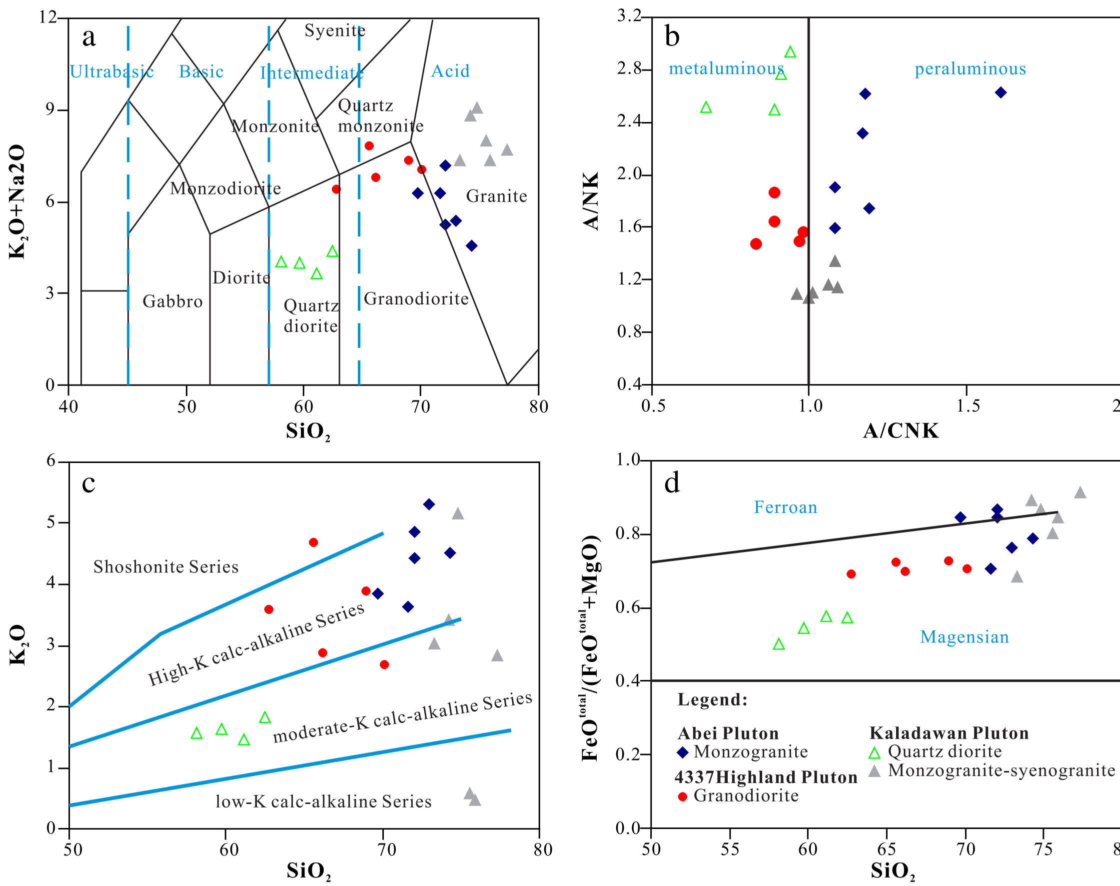

Fig. 7. Chemical classification diagrams for these plutons. (a) (K_2O + Na_2O) versus SiO_2 diagram; (b) A/CNK versus A/NK diagram; (c) SiO_2 versus K_2O diagram; (d) FeO^{total} / (FeO^{total} + MgO) versus SiO_2 diagram (after Frost and Frost, 2008).

Pluton are rare. Secondly, the melts produced from the partial melting of oceanic slab are Na-rich and have high $Mg^{\#}$ (>50), Cr (>50 ppm), and Ni (>20 ppm) due to interaction with the mantle wedge (Condie, 2005b; Defant and Drummond, 1990); this is inconsistent with the 4337 Highland Pluton. Meanwhile, the subducted oceanic slab in NAOB may be too cold to form pluton derived from the melting of oceanic slab (Zhang and Meng, 2006; Zhang et al., 2015). Thirdly, the trace elements of 4337 Highland Pluton showed in Fig. 8c and d do resemble the crustal values (Rudnick and Gao, 2003). So the possible partial melting origins include thickened lower continental crust and delaminated lower continental crust. Although the wide range $\varepsilon_{Hf}(t)$ values (from negative to weakly positive) suggest the contamination of mantle magma, it is different from the high-Mg adakitic rocks which have highly positive $\varepsilon_{Hf}(t)$ values (e.g. Yu et al., 2015) sourced from delaminated lower continental crust. Therefore the 4337 Highland Pluton was most likely derived from partial melting of thickened lower continental crust.

A series of partial melting experiments demonstrated that the high-pressure partial melting of metabasalt or eclogite can produce melts with garnet-bearing plagioclase-poor residues (Huang and He, 2010; Laurie and Stevens, 2012; Rapp, 1995; Rapp and Watson, 1995), which is in harmony with the geochemistry of the 4337 Highland Pluton (e.g., weakly negative Eu anomaly and higher $(La/Yb)_N$). Moreover, The Nb/Ta ratio (10.86–18.93) of the 4337 Highland Pluton suggests that the Ti-bearing mineral is rutile rather than titanite in the residue (John et al., 2011). And some researchers have proposed that the residual rutile is accounted for high-pressure (>15 kbar) melting and that continental crustal thickness is >50 km (Xiong et al., 2005, Xiong, 2006). It has been proposed that the plagioclase-out curve has a negative dP/dT slope for temperatures lower than 900 °C (Qian and Hermann, 2013). In our case, the magma is saturated due to the existence of 675 Ma inherited zircon (Fig. 4; Table 1) which means that the temperature (737–796 °C) calculated by zircon saturation thermometer (Boehnke et al., 2013) is maxima estimate (Miller et al., 2003). So the presence of a minor plagioclase residue exhibited by a weakly negative Eu anomaly in 4337 Highland Pluton (Fig. 8c) is reasonable under the condition of <770 °C and ~15 kbar. And the negative Ba anomaly and strongly positive Th anomaly (Fig. 8d) are inherited from the lower continental crust (e.g. Wang et al., 2005). Meanwhile, the partial melting of thickened lower continental crust at high pressure also requires a significant amount of water (Condie, 2005b), which is in harmony with the fact that 4337 Highland Pluton has more normative anorthite than orthoclase (Conrad et al., 1988) as shown in the An-Ab-Or diagram (Fig. 10a).

As mentioned above, the 4337 Highland Pluton was produced by the high-pressure fluid-present melting of thickened lower continental crust with a residue dominated by garnet along with minor plagioclase and rutile.

5.1.3. Kaladawan Pluton

The quartz diorites of the Kaladawan Pluton have lower SiO_2, K_2O and higher Mg, Ni, Co relative to the monzogranite–syenogranite of this pluton (Fig. 7; Table 3), implying a mantle source. Based on the zircon $\varepsilon_{Hf}(t)$ values ($\varepsilon_{Hf}(t)$ = +5.4 to +8.5, Fig. 6) and the younger second-stage model age (Table 2), we explain that they were chiefly from depleted lithospheric mantle. The relatively low $Mg^{\#}$ implies

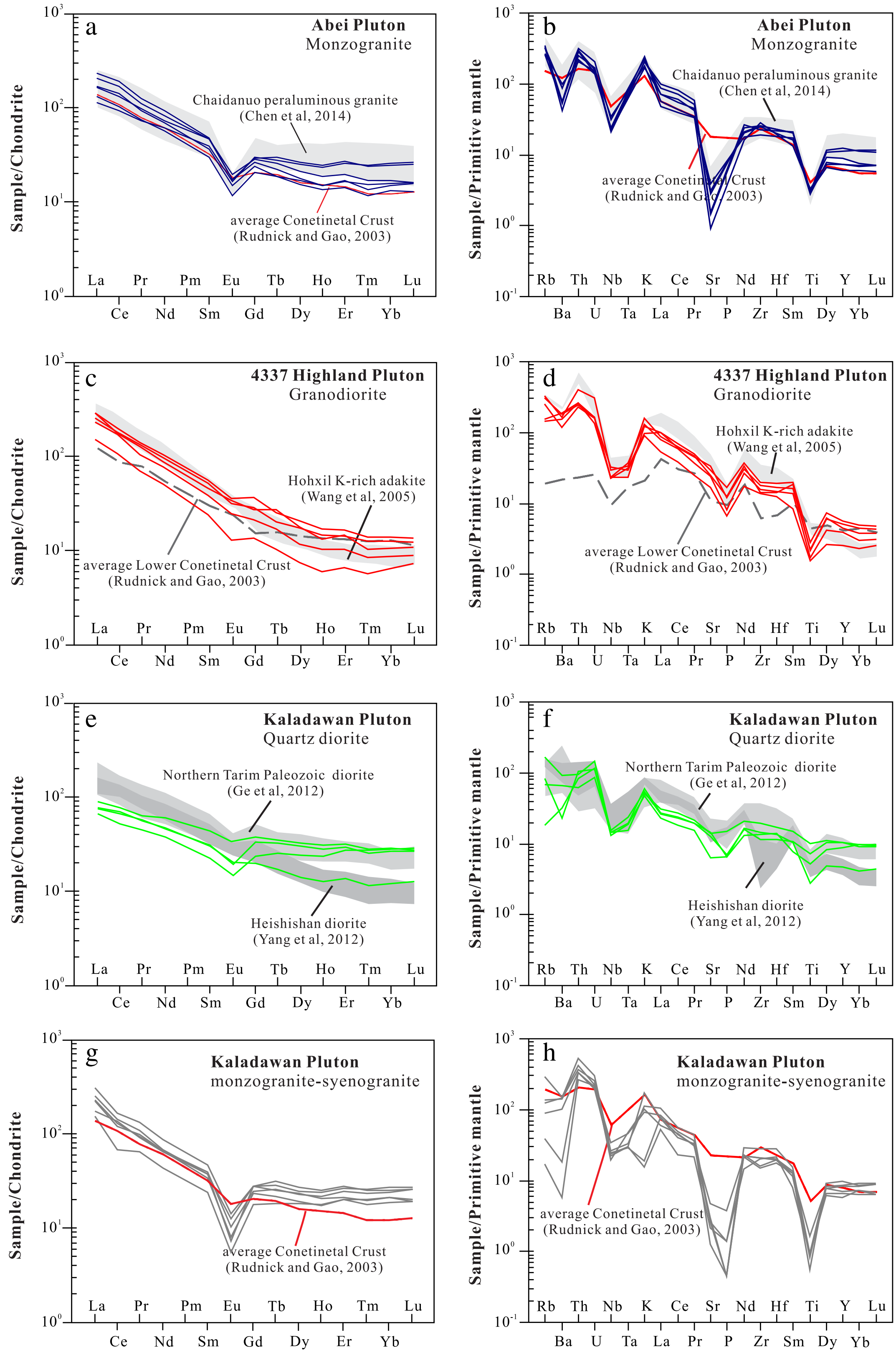

Fig. 8. Chondrite-normalized REE element patterns and primitive mantle-normalized trace element spider diagrams for the Abei Pluton (a, b), the 4337 Highland Pluton (c, d) and the Kaladawan Pluton (e–h). Normalization values are from Sun and McDonough (1989). The data for average continental crust and lower continental crust are from Rudnick and Gao (2003). The shaded areas is the magmatic rocks from other study area (Chen et al., 2014; Ge et al., 2012; Wang et al., 2005; Yang et al., 2012), which have similar trace elements characteristics with our samples.

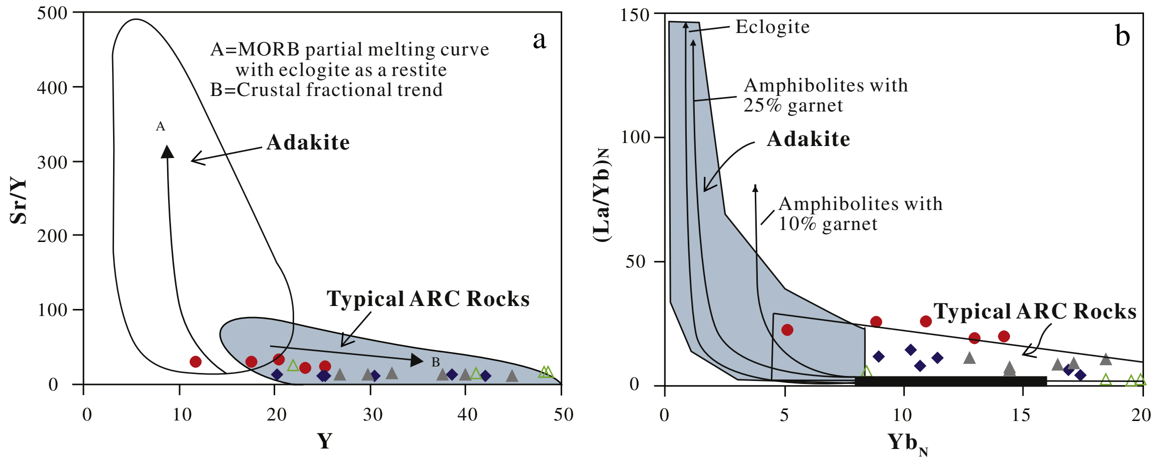

Fig. 9. (a) Sr/Y versus Y diagram and (b) $(La/Yb)_N$ versus Yb_N for the graintoids in the NAOB. The fields for adakite and magmatic arc rocks are from Defant and Drummond (1990). Symbols are same as in Fig. 7.

that the magmas were not primary and the Ta/Yb–Th/Yb diagram (Fig. 10b) reveals that they have experienced the process of fractional crystallization (e.g. Pearce et al., 1990). Given the abundance of these elements in the continental crust (Ge et al., 2012; Sivell and Waterhouse, 1988; Yang et al., 2015), the moderate-K calc-alkaline together with low Ba, Sr and negative Zr, Hf anomalies of the pluton show that crustal assimilation was insignificant; this is consistent with the lack of inherited zircons and limited range of $\varepsilon_{Hf}(t)$ values. And the fluid derived from subducted oceanic slab dehydration enters the overlying mantle wedge (Fig. 10a) which triggers melting of the mantle wedge and leads to a slight enrichment of LREEs compared with HREEs, and an enrichment of LILEs (e.g., Rb, Th, U) compared with HFSEs (e.g., Nb, Ta, Y) (Fig. 8e–f).

The geochemical characteristics of the monzogranite–syenogranite of the Kaladawan Pluton are accounted for a crustal origin. It is turned out that there was minor sediment in the source area because these rocks have a lower Al_2O_3 content and are metaluminous (Chappell and White, 1992; Zen, 1986). And the low Sr/Y ratio and strongly negative Eu anomaly are deciphered an origin by partial melting of meta-igneous rocks in the shallow continental crust (i.e., at low pressure) with a plagioclase-rich, garnet-free residue (Patiño Douce and Beard, 1995). The different Hf istopic compositions among the quartz diorite and monzogranite–syenogranite from the Kaladawan Pluton imply they could derive from different source. Relative to the highly positive $\varepsilon_{Hf}(t)$ values of quartz diorite, the weakly positive $\varepsilon_{Hf}(t)$ values of monzogranite– syenogranite are interpreted that they were derived from decompression partial melting of Neoproterozoic continental crust mixing the juvenile underplated mafic material from the depleted lithospheric mantle. Likewise, the positive correlations among the K_2O, Rb/Sr and Th/Ta ratios from the quartz diorite to the monzogranite–syenogranite (Fig. 11) reveal the fact that the greater amount of continental components present during partial melting (e.g. Brown et al., 1984; Elliott et al., 1997; Poli et al., 1989; Wilson, 2007).

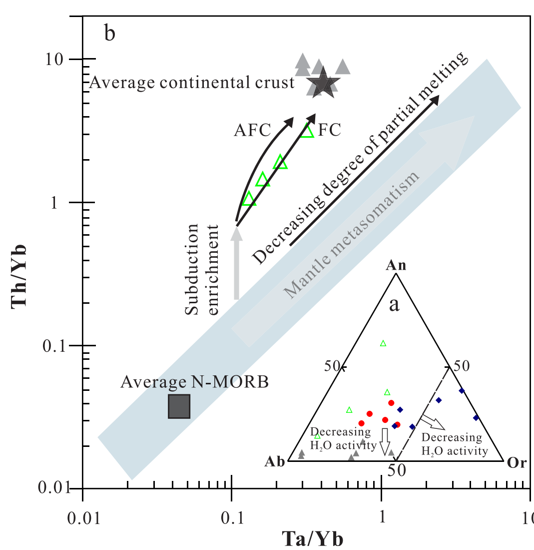

Fig. 10. (a) Ab–Or–An tertiary diagram (after Conrad et al., 1988). The arrow indicates the trend with decreasing water activity. (b) Th/Yb versus Ta/Yb diagram (after Pearce et al., 1990) for the Kaladawan Pluton. Average N-MORB composition and average continental crust are from Sun and McDonough (1989) and Rudnick and Gao (2003), respectively. Arrows show the trends for fractional crystallization (FC), assimilation–fractional crystallization (AFC), subduction enrichment and mantle metasomatism. Symbols are same as in Fig. 7.

5.2. Tectonic implications

5.2.1. Initiation of subduction

In general, a granitic magma derived under low-pressure and high-temperature conditions forms during an anorogenic stage with upwelling of asthenosphere (Barbarin, 1999; Bonin, 2007; Sylvester, 1998). However, the age of the Abei Pluton (ca. 514 Ma) is inconsistent with such a setting, because the anorogenic stage of the NAOB began at 440 Ma (Meng et al., 2016). The age of 514 Ma is earlier than that of previously reported subduction-related granitoids (510–460 Ma) in the NAOB (Gehrels et al., 2003a; Han et al., 2012; Qi et al., 2005a; Wu et al., 2005, 2007), indicating a subduction model is a more appropriate explanation for the origin of the Abei Pluton. Because the NAOB is the westward continuation of the North Qilan Orogenic Belt and has the same tectonic history as the latter at the period of Paleozoic (Zhang et al., 2014), the similarity between Abei Pluton and Chaidanuo granite in the North Qilian (Chen et al., 2014) indicates that the former also formed during the initial stages of subduction. This view is in harmony with the Abei Pluton being older than the supra subduction zone (SZZ) type ophiolites (Liu et al., 2013; Wu et al., 2002; Xiu et al., 2007; Yang et al., 2008) and eclogites (Zhang et al., 2005, Zhang et al., 2015) in NAOB, but is contemporaneous with tholeiitic basalt (517 Ma, unpublished data of authors) which is thought to be the product of subduction initiation (e.g. Todd et al., 2012).

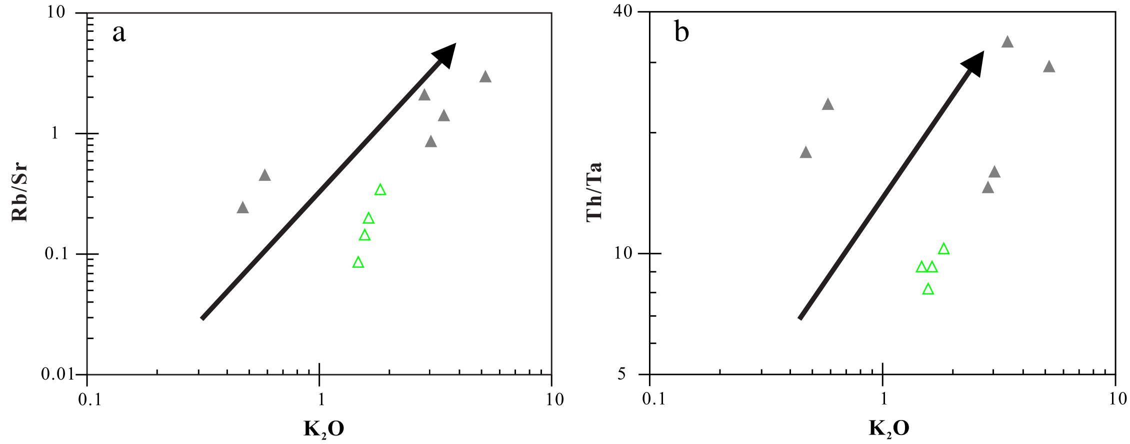

Fig. 11. (a) K_2O versus Rb/Sr diagram and (b) K_2O versus Th/Ta diagram for the Kaladawan Pluton. Arrows show the trend with increasing maturity of the arc. Symbols are same as in Fig. 7.

During the initial stages of subduction, oceanic crust was subducted beneath the CAB at a steep angle and subduction hinge "pull-back" occurred because the velocity of oceanic slab rollback exceeded that of the overriding plate (Cawood et al., 2009; Lister and Forster, 2009). In this case, oceanic slab rollback induced lithospheric extension and upwelling of asthenosphere which caused thinning and partial melting of the continental crust of the CAB to form the Abei Pluton (e.g. Collins, 2002; Collins and Richards, 2008). Although the source of heat comes from the underplating of mantle-derived magma, our $\varepsilon_{Hf}(t)$ values make clear that the contribution of mantle materials is insignificant.

5.2.2. Flat subduction

Generally speaking, there are two likely tectonic settings that could account for melts derived from partial melting of thickened lower continental crust. One is the anorogenic stage during which the previously thickened lower continental crust delaminated or foundered (Gao et al., 2004; He et al., 2011; Hou et al., 2004; Xu et al., 2002; Yu et al., 2015); the other is flat-slab subduction in which partial melting of thickened lower continental crust is caused by the presence of external fluid (Li and Li, 2007; Zhu et al., 2013). As seen Section 5.1.2, the adakitic melts derived from the delaminated lower continental crust typically have a high $Mg^{\#}$ and postive $\varepsilon_{Hf}(t)$ values(Gao et al., 2004; Xu et al., 2002), whereas the 4337 Highland Pluton does not. So the flat-slab subduction is an appropriate explanation in this case given the age constraints. In addition, flat subduction can result in strike-slip motion and fold–thrust belts (Cawood et al., 2009; Collins, 2002); our field investigations revealed the compressional deformation is predominant during 500–490 Ma in study area, such as the widely developed NWW-striking plunging-vertical fold. The absence of 500–490 Ma volcanic rocks (i.e., a volcanic gap) is also a typical trait of flab subduction, which is similar to the case in the Central Andes during the late Miocene (Kay and Abbruzzi, 1996; Kay et al., 2005; Ramos and Folguera, 2009). Comparison of the Abei Pluton and the 4337 Highland Pluton reveals the latter has higher Gd/Yb ratios at a given La/Sm value (Fig. 12) and equilibrates with a plagioclase-free reside containing abundant garnet. These characteristics also suggest that the continental crust thickened from ca. 520 Ma to ca. 500 Ma (e.g., Kay and Abbruzzi, 1996).

Another question to consider is how the continental crust thickened during flat subduction. The flat-slab subduction caused the lithosphere of CAB to be in overall contraction because the velocity of the overriding plate exceeded that of oceanic slab rollback (Cawood et al., 2009; Lister and Forster, 2009); this contraction also induce the increase of continental crust thickness. For example, the crustal thickness beneath the Andean Precordillera during flat-slab subduction locally exceeds 60 km according to seismic data (Luján et al., 2015).

5.2.3. Tectonic model

According to the differences in geochemical characteristics and magma type between continental magmatic arcs and island magmatic arcs (Wilson, 2007), previous authors proposed the existence of a continental arc belt along the northern margin of the CAB during the Late Cambrian to Early Ordovician (Hao et al., 2006; Zhang et al., 2015). In our new tectonic model (Fig. 13), we propose that the angle of subduction changed during 520–460 Ma, and we reconstruct this evolutional history.

Fig. 13a shows the initiation of the southward subduction of oceanic crust beneath the CAB at ca. 514 Ma. The buoyancy contrast between the subducted oceanic slab and the overriding plate results in spontaneous steep-angle subduction (Stern, 2004; Niu et al., 2003). The negatively buoyant oceanic crust sinks at a steep angle beneath the continental crust, as it became older and colder as it migrated away from the oceanic spreading ridge where it formed (Stern, 2004; Niu et al., 2003; Chen et al., 2014).

With ongoing subduction, the oceanic slab becomes heavier and the rollback velocity increases. Consequently, lithospheric extension of overriding plate accompanying the upwelling of asthenosphere causes continental crust thinning and partial melting, leading to the formation

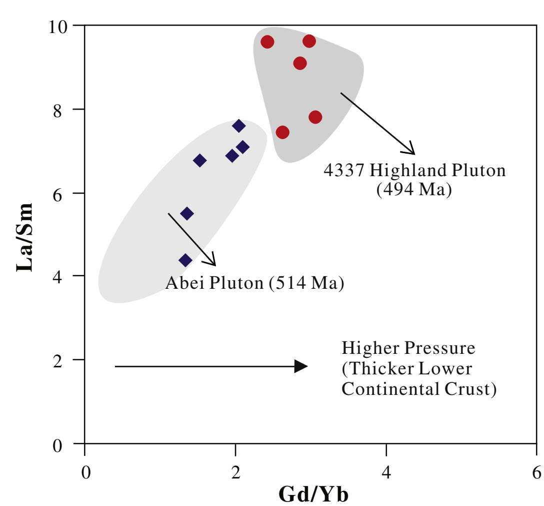

Fig. 12. Gd/Yb versus La/Sm diagram for Abei Pluton and 4337 Highland Pluton. The higher La/Sm ratios at a given Gd/Yb are best explained by a higher formation pressure, which is determined by the thickness of continental crust. Symbols are same as in Fig. 7.

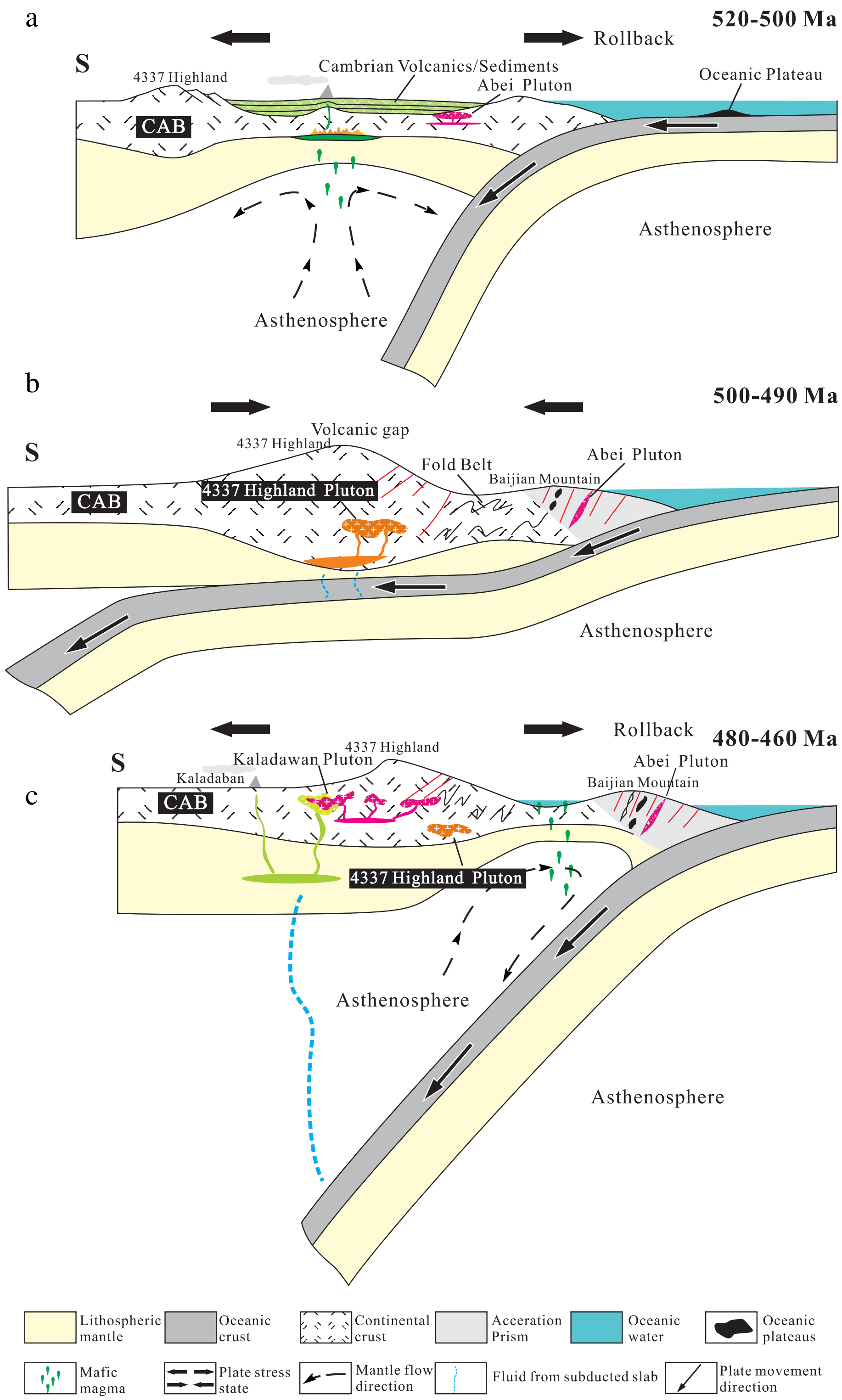

Fig. 13. Schematic model of the tectonic evolution of the NAOB during the 520–460 Ma, which account for the petrogenesis of the Abei, 4337 Highland and Kaladawan Plutons.

of the Abei Pluton. This process also triggers the decompression melting of lithospheric mantle to form the underplating of basalt (Todd et al., 2012); e.g., the 517 Ma tholeiitic basalt to the southern part of the Abei Pluton (unpublished data of authors).

As shown in Fig. 13b, the arrival of an oceanic plateau or aseismic ridge with positive buoyancy makes the subducted oceanic slab become light to induce the transition from steep-angle subduction to flat-slab subduction (Collins, 2002; Collins and Richards, 2008; Li and Li, 2007; Kay et al., 2005; Lister and Forster, 2009). This process was accompanied by crustal thickening, subduction erosion, the southward migration of magmatic activity, intense transpressional deformation (e.g., the plunging-vertical fold) and a volcanic gap. The Abei Pluton may have been squeezed into the accretionary prism by the thrust-fault caused by intense compression. And the partial melting of thickened lower continental crust form the 4337 Highland Pluton with the influx of fluid. With ongoing flat-slab subduction, the eclogitization caused the oceanic slab to sink, roll back and even break-off (Collins and Richards, 2008; Li and Li, 2007). Consequently, flat-slab subduction is always short-lived (ca. 10 m. y.) and evolves to steep-angle subduction again.

As the subduction angle of the oceanic slab increased during 480–460 Ma, the continental volcanic arc was reestablished and migrated south to the Kaladaban District (Fig. 13c); e.g., the volcanic belt related to the VMS Pb–Zn deposits (Chen et al., 2015). The transition from contraction to extension as a result of oceanic slab rollback caused the upwelling of asthenosphere and partial melting of the mantle wedge to form the quartz diorite. Subsequently the mantle-derived magma underplate the basement of CAB, providing heat and material for partial melting of continental crust to form the monzogranite–syenogranite of Kaladawan Pluton. Moreover, according to the $\varepsilon_{Hf}(t)$ values vary from negative to positive in the NAOB at ca.520–460 Ma, we suggest the ancient lower continental crust in the CAB was gradually replaced by mantle-derived juvenile materials.

6. Conclusions

The Abei, 4337 Highland and Kaladawan Plutons successively expose and become younger from north to south in the North Altun orogenic belt. Their magma crystallization ages are 514.3 ± 5.6 Ma, 494.4 ± 5.5 Ma and 480–460 Ma, respectively. The geochemical and isotopic traits show they are derived from different sources under various P-T conditions.

According to above characteristic and previous data, we propose a new model in which the subduction angle changed during the 520–460 Ma. The initiation of subduction occurred during 520–500 Ma causes the lithospheric extension, asthenosphere upwelling and dehydration melting of the continental crust to form the Abei Pluton. Subsequent transition from steep-angle to flat-slab subduction at ca.500 Ma, due to the arrival of buoyant oceanic plateaus, induces the lithospheric contraction and the thickened continental crust. With the influx of fluid, the 4337 Highland Pluton is derived from the partial melting of thickened lower continental crust. With ongoing subduction, the steep-angle subduction system is reestablished to cause the decompression partial melting of depleted mantle and continental crust to form the 480–460 Ma Kaladawan Pluton.

Acknowledgements

We thank two anonymous reviewers for their extremely useful comments which significantly improved our paper. The work was financially supported by the Key Projects in the National Science & Technology Pillar Program (No. 2006BAB07B02-04 and 2011BAB06B08-04) and the Geological Survey Project of China (No. 1212011085043).

References

Atherton, M.P., Petford, N., 1993. Generation of sodium-rich magmas from newly underplated basaltic crust. Nature 362, 144–146.

Barbarin, B., 1999. A review of the relationship between granitioid types, their origins and their geodynamic environments. Lithos 46, 605–626.

Barnes, C.G., Petersen, S.W., Kistler, R.W., Murray, R., Kays, M.A., 1996. Source and tectonic implications of tonalite-trondhjemite magmatism in the Klamath Mountains. Contributions to Mineralogy and Petrology 123, 40–60.

Boehnke, P., Waston, E.B., Trail, D., Harrison, T.M., Schmitt, A.K., 2013. Zircon saturation re-revisited. Chemical Geology 351, 324–334.

Bonin, B., 2007. A-type granites and related rocks: evolution of a concept, problems and prospects. Lithos 97, 1–29.

Bouvier, A., Vervoort, J.D., Patchett, P.J., 2008. The Lu–Hf and Sm–Nd isotopic composition of CHUR: constraints from unequilibrated chondrites and implications for the bulk composition of terrestrial planets. Earth and Planetary Science Letters 273, 48–57.

Brown, G.C., Thorpe, R.S., Webb, P.C., 1984. The geochemical characteristics of granitoids in contrasting arcs and comments on magma sources. Journal of the Geological Society 141, 413–426.

Cao, Y.T., Liu, L., Wang, C., Yang, W.Q., Zhu, X.H., 2010. Geochemical, zircon U-Pb dating and Hf isotope composition studies for Tatelekebulake granite in south Altyn Tagh. Acta Petrologica Sinica 26, 3259–3271 (in Chinese with English abstract).

Castillo, P.R., Janney, P.E., Solidum, R.U., 1999. Petrology and geochemistry of Camiguin island, southern Philippines: insights to the source of adakites and other lavas in a complex arc setting. Contributions to Mineralogy and Petrology 134, 33–51.

Cawood, P.A., Kröner, A., Collins, W.J., Kusky, T.M., Mooney, W.D., Windley, B.F., 2009. Accretionary orogens through Earth history. Geological Society, London, Special Publications 318, 1–36.

Chappell, B.W., White, A.J.R., 1992. I and S type granites in the Lachlan Fold Belt. Transactions of the Royal Society of Edinburgh: Earth Sciences 83, 1–26.

Chappell, B.W., Wyborn, D., 2012. Origin of enclaves in S-type granites of the Lachlan Fold Belt. Lithos 154, 235–247.

Chen, Y.X., Song, S.G., Niu, Y.L., Wei, C.J., 2014. Melting of continental crust during subduction initiation: a case study from the Chaidanuo peraluminous granite in the North Qilian suture zone. Geochimica et Cosmochimica Acta 132, 311–336.

Chen, B.L., Wang, Y., Chen, Z.L., Li, S.B., Jiang, R.B., Han, F.B., Cui, L.L., Li, L., Zhao, S.M., Qi, W.X., Yang, Y., Wang, S.X., Zhou, Y.G., Hao, R.X., 2015. A study of the structural system of ore-forming and ore-controlling in Kaladawan ore clustering area, Altun Tagh mountains, NW China. Earth Science Frontiers 22, 67–77 (in Chinese with English abstract).

Chiaradia, M., Müntener, O., Beate, B., Fontignie, D., 2009. Adakite-like volcanism of Ecuador: lower crust magmatic evolution and recycling. Contributions to Mineralogy and Petrology 158, 563–588.

Chu, N.C., Taylor, R.N., Chavagnac, V., Nesbitt, R.W., Boella, R.M., Milton, J.A., German, C.R., Bayon, G., Burton, K., 2002. Hf isotope ratio analysis using multi-collector inductively coupled plasma mass spectrometry: an evaluation of isobaric interference corrections. Journal of Analytical Atomic Spectrometry 17, 1567–1574.

Clemens, J.D., 2003. S-type granitic magmas-petrogenetic issues, models and evidence. Earth Science Reviews 61, 1–18.

Collins, W.J., 2002. Hot orogens, tectonic switching, and creation of continental crust. Geology 30, 535–538.

Collins, W.J., Richards, S.W., 2008. Geodynamic significance of S-type granites in circum-Pacific orogens. Geology 36, 559–562.

Condie, K.C., 2005a. Earth as an Evolving Planetary System. Elsevier Academic, London, pp. 78–90.

Condie, K.C., 2005b. TTGs and adakites: are they both slab melts? Lithos 80, 33–44.

Conrad, W.K., Nicholls, I.A., Wall, V.J., 1988. Water-saturated and -undersaturated melting of metaluminous and peraluminous crustal compositions at 10 kb: evidence for the origin of silicic magmas in the Taupo Volcanic Zone, New Zealand, and other occurrences. Journal of Petrology 29, 765–803.

Defant, M.J., Drummond, M.S., 1990. Derivation of some modern arc magmas by melting of young subducted lithosphere. Nature 347, 662–665.

Elliott, T., Plank, T., Zindler, A., White, W., Bourdon, B., 1997. Element transport from slab to volcanic front at the Mariana arc. Journal of Geophysical Research 102, 14991–15019.

Frost, B.R., Frost, C.D., 2008. A geochemical classification for feldspathic igneous rocks. Journal of Petrology 49, 1955–1969.

Gao, S., Rudnick, R.L., Yuan, H.L., Liu, X.M., Liu, Y.S., Xu, W.L., Ling, W.L., Ayers, J., Wang, X.C., Wang, Q.H., 2004. Recycling lower continental crust in the North China craton. Nature 432, 892–897.

Ge, R.F., Zhu, W.B., Wilde, S.A., He, J.W., Cui, X., Wang, X., Zheng, B.H., 2012. Neoproterozoic to Paleozoic long-lived accretionary orogeny in the northern Tarim Craton. Tectonics 33, 302–329.

Gehrels, G.E., Yin, A., Wang, X.F., 2003a. Magmatic history of the northeastern Tibetan plateau. Journal of Geophysical Research 108, 2423.

Gehrels, G.E., Yin, A., Wang, X.F., 2003b. Detrital-zircon geochronology of the northeastern Tibetan plateau. Geological Society of America Bulletin 115, 881–896.

Green, T.H., 1995. Significance of Nb/Ta as an indicator of geochemical processes in the crust-mantle system. Chemical Geology 120, 347–359.

Griffin, W.L., Pearson, N.J., Belousova, E., Jackson, S.E., van Achterbergh, E., O'Reilly, S.Y., Shee, S.R., 2000. The Hf isotope composition of cratonic mantle: LA-MC-ICPMS analysis of zircon megacrysts in kimberlites. Geochimica et Cosmochimica Acta 64, 133–147.

Griffin, W.L., Wang, X., Jackson, S.E., Pearson, N.J., O'Reilly, S.Y., Xu, X.S., Zhou, X.M., 2002. Zircon chemistry and magma mixing, SE China: in situ analysis of Hf isotopes, Tonglu and Pingtan igneous complexes. Lithos 61, 237–269.

Guo, Z.J., Yin, A., Robinson, A.C., Jia, C.Z., 2005. Geochronology and geochemistry of deep-drill-core samples from the basement of the central Tarim basin. Journal of Asian Earth Sciences 25, 45–56.

Han, F.B., Chen, B.L., Cui, L.L., Wang, S.X., Chen, Z.L., Jiang, R.B., Li, L., Qi, W.X., 2012. Zircon SHRIMP U-Pb age of intermediate-acid intrusive rocks in Kaladawan area, eastern Altun mountains, NW China, and its implications. Acta Petrologica Sinica 28, 2271–2281 (in Chinese with English abstract).

Hao, J., Wang, E.Q., Liu, X.H., Sang, H.Q., 2006. Jinyanshan collisional oroginic belt of the early Paleozoic in the Altun mountains: evidence from single zircon U-Pb and ^{40}Ar-^{39}Ar isotopic dating for the arc magmatite and ophiolitic mélange. Acta Petrologica Sinica 22, 2743–2752 (in Chinese with English abstract).

He, Y.S., Li, S.G., Hoefs, J., Huang, F., Liu, S.A., Hou, Z.H., 2011. Post-collisional granitoids from the Dabie orogeny: new evidence for partial melting of a thickened continental crust. Geochimica et Cosmochimica Acta 75, 3815–3838.

Hou, Z.Q., Gao, Y.F., Qu, X.M., Rui, Z.Y., Mo, X.X., 2004. Origin of adakitic intrusives generated during mid-Miocene east-west extension in southern Tibet. Earth and Planetary Science Letters 220, 139–155.

Huang, F., He, Y.S., 2010. Partial melting of the dry mafic continental crust: implications for petrogenesis of C-type adakites. Chinese Science Bulletin 55, 1255–1267.

John, T., Klemd, R., Klemme, S., Pfänder, J.A., Hoffmann, J.E., Gao, J., 2011. Nb-Ta fractionation by partial melting at the titanite–rutile transition. Contributions to Mineralogy and Petrology 161, 35–45.
Kay, S.M., Abbruzzi, J.M., 1996. Magmatic evidence for Neogene lithospheric evolution of the central Andean "flat-slab" between 30 °S and 32 °S. Tectonophysics 259, 15–28.
Kay, S.M., Mpodozis, C., 2001. Central Andean ore deposits linked to evolving shallow subduction systems and thickening crust. Geological Society of America Bulletin 11, 4–9.
Kay, S.M., Godoy, E., Kurtz, A., 2005. Episodic arc migration, crustal thickening, subduction erosion, and magmatism in the south-central Andes. Geological Society of America Bulletin 117, 67–88.
Laurie, A., Stevens, G., 2012. Water-present eclogite melting to produce Earth's early felsic crust. Chemical Geology 314-317, 83–95.
Li, Z.X., Li, X.H., 2007. Formation of the 1300-km-wide intracontinental orogen and postorogenic magmatic province in Mesozoic south China: a flat-slab subduction model. Geology 35, 179–182.
Lister, G., Forster, M., 2009. Tectonic mode switches and the nature of orogenesis. Lithos 113, 274–291.
Liu, L., Zhang, A.D., Chen, D.L., Yang, J.X., Luo, J.H., Wang, C., 2007. Implications based on LA-ICP-MS zircon U-Pb ages of eclogite and its country rock from Jianggalesayi area, Altyn Tagh. Earth Science Frontiers 14, 98–107.
Liu, L., Wang, C., Chen, D.L., Zhang, A.D., Liou, J.G., 2009. Petrology and geochronology of HP-UHP rocks from the South Altyn Tagh, northwestern China. Journal of Asian Earth Sciences 35, 232–244.
Liu, H., Wang, G.C., Yang, Z.J., Luo, Y.J., Gao, R., Huang, W.X., 2013. Geochronology and geochemistry of the Qiashikansayi basalt and its constraint on the closure progress of the North Altyn Ocean. Acta Geologica Sinica 87, 38–54 (in Chinese with English abstract).
Long, X.P., Yuan, C., Sun, M., Kröner, A., Zhao, G.C., 2014. New geochemical and combined zircon U-Pb and Lu-Hf isotopic data of orthogneisses in the northern Altyn Tagh, northern margin of the Tibetan plateau: implication for Archean evolution of the Dunhuang Block and crust formation in NW China. Lithos 200-201, 418–431.
Lu, S.N., Li, H.K., Zhang, C.L., Niu, G.H., 2008. Geological and geochronological evidence for the Precambrian evolution of the Tarim Craton and surrounding continental fragments. Precambrian Research 160, 94–107.
Ludwig, K.R., 2003. User's Manual for Isoplot 3.0: a Geochronological Toolkit for Microsoft Excel. 4. Berkeley Geochronology Center Special Publication, pp. 1–71.
Luján, S.B.P., Ammirati, J.B., Alvarado, P., Vujovich, G.I., 2015. Constraining a mafic thick crust model in the Andean Precordillera of the Pampean flat slab subduction region. Journal of South American Earth Sciences 64, 325–338.
Meng, L.T., Chen, B.L., Wang, Y., Sun, Y., Wu, Y., Zhang, W.G., He, J.T., 2016. The timing of Early Paleozoic regime transition of the North Altyn Tagh area: the evident from granite. Geotectonica et Metallogenia 141, 1–15 (in Chinese with English abstract).
Miller, C.F., McDowell, S.M., Mapes, R.W., 2003. Hot and cold granites? Implications of zircon saturation temperatures and preservationof inheritance. Geology 31, 529–532.
Niu, Y.L., O'Hara, M.J., Pearce, J.A., 2003. Initiation of subduction zones as a consequence of lateral compositional buoyancy contrast within the lithosphere: a petrological perspective. Journal of Petrology 44, 851–866.
Patiño Douce, A.E., 1995. Experimental generation of hybrid silicic melts by reaction of high-Al basalt with metamorphic rocks. Journal of Geophysical Research 100, 15623–15639.
Patiño Douce, A.E., Beard, J.S., 1995. Dehydration-melting of biotite gneiss and quartz amphibolite from 3 to 15 kbar. Journal of Petrology 36, 707–738.
Pearce, J.A., Bender, J.F., De Long, S.E., Kidd, W.S.F., Low, P.J., Güner, Y., Şaroğlu, F., Yilmaz, Y., Moorbath, S., Mitchell, J.J., 1990. Genesis of collision volcanism in eastern Anatolia, Turkey. Journal of Volcanology and Geothermal Research 44, 189–229.
Poli, G., Ghezzo, C., Conticelli, S., 1989. Geochemistry of granitic rocks from the Hercynian Sardinia-,Corsica batholith: implication for magma genesis. Lithos 23, 247–266.
Qi, X.X., Li, H.B., Wu, C.L., Yang, J.S., Zhang, J.X., Meng, F.C., Shi, R.D., Chen, S.Y., 2005a. SHRIMP U-Pb age of zircons from qiashikasayi granodiorite in the northern Alty Tagh mountains and its significations. Chinese Science Bulletin 50, 571–576 (in Chinese with English abstract).
Qi, X.X., Wu, C.L., Li, H.B., 2005b. SHRIMP U-Pb age of zircons from kazisayi granite in the northern Alty Tagh mountains and its significations. Acta Petrologica Sinica 21, 859–866 (in Chinese with English abstract).
Qian, Q., Hermann, J., 2013. Partial melting of lower crust at 10-15 kbar: constraints on adakite and TTG formation. Contributions to Mineralogy and Petrology 165, 1195–1224.
Ramos, V.A., Folguera, A., 2009. Andean flat-slab subduction through time. Geological Society, London, Special Publications 327, 31–54.
Ramos, V.A., Cristallini, E.O., Daniel, J.P., 2002. The Pampean flat-slab of Central Andes. Journal of South American Earth Sciences 15, 59–78.
Rapp, R.P., 1995. Amphibole-out phase boundary in partially melted metabasalt, its control over liquid fraction and composition, and source permeability. Journal of Geophysical Research 100, 15601–15610.
Rapp, R.P., Watson, E.B., 1995. Dehydration melting of metabasalt at 8–32 kbar: implications for continental growth and crust–mantle recycling. Journal of Petrology 36, 891–931.
Rapp, R.P., Shimizu, N., Norman, M.D., Applegate, G.S., 1999. Reaction between slab-derived melts and peridotite in the mantle wedge: experimental constraints at 3.8 GPa. Chemical Geology 160, 335–356.
Ritts, B.D., Biffi, U., 2000. Magnitude of post-middle Jurassic (Bajocian) displacement on the central Altyn Tagh fault system, northwest China. Geological Society of America Bulletin 112, 61–74.
Rudnick, R.L., Gao, S., 2003. Composition of the Continental Crust. Elsevier-Pergamon Oxford, pp. 1–62.
Scherer, E., Munker, C., Mezger, K., 2001. Calibration of the lutetium-hafnium clock. Science 293, 683–687.
Sen, C., Dunn, T.D., 1994. Dehydration melting of a basaltic composition amphibolites at 1.5 and 2.0 GPa: implications for the origin of adakites. Contributions to Mineralogy and Petrology 117, 394–409.
Sivell, W.J., Waterhouse, J.B., 1988. Petrogenesis of Gympie Group volcanics: evidence for remnants of an early Permian volcanic arc in eastern Australia. Lithos 21, 81–95.
Sobel, E.R., Arnaud, N., 1999. A possible middle Paleozoic suture in the Altyn Tagh, NW China. Tectonics 18 (1), 64–74.
Song, B., Zhang, Y.H., Wan, Y.S., Jian, P., 2002. Mount making and procedure of the SHRIMP dating. Geology Review 48, 26–30 (in Chinese with English abstract).
Stern, R.J., 2004. Subduction initiation: spontaneous and induced. Earth and Planetary Science Letters 226, 275–292.
Sun, S.S., McDonough, W.F., 1989. Chemical and isotopic systematics of oceanic basalts: implications for mantle composition and processes. Geological Society of London, Special Publication 42, 313–345.
Sylvester, P.J., 1998. Post-collisional peraluminous granites. Lithos 45, 29–44.
Sylvester, P.J., Campbell, I.H., Bowyer, D.A., 1997. Niobium/uranium evidence for early formation of the continental crust. Science 275, 521–523.
Tatsumi, Y., Kogiso, T., 2003. The subduction factory: it's role in the evolution of the Earth's mantle. Geological Society of London, Special Publication 219 (1), 55–80.
Todd, E., Gil, J.B., Pearce, J.A., 2012. A variably enriched mantle wedge and contrasting melt types during arc stages following subduction initiation in Fiji and Tonga, southwest Pacific. Earth and Planetary Science Letters 335-336, 180–194.
Wang, Q., McDermott, F., Xu, J.F., Bellon, H., Zhu, Y.T., 2005. Cenozoic K-rich adakitic volcanic rocks in the Hohxil area, northern Tibet: lower-crustal melting in an intracontinental setting. Geology 33, 465–468.
Wang, C., Liu, L., Yang, W.Q., Zhu, X.H., Cao, Y.T., Kang, L., Chen, S.S., Li, R.S., He, S.P., 2013. Provenance and ages of the Altyn Complex in Altyn Tagh: implications for the early Neoproterozoic evolution of northwestern China. Precambrian Research 230, 193–208.
Wilson, M., 2007. Igneous Petrogenesis: a Global Tectonic Approach. Chapman Hall, London, pp. 191–225.
Wu, J., Lan, C.L., Li, J.L., Yu, L.J., 2002. Geochemical evidence of MORB and OIB combination in Hongliugou ophiolite melanges, Altun fault belt. Scientia Geologica Sinica 21, 24–30 (in Chinese with English abstract).
Wu, C.L., Yang, J.S., Yao, S.Z., Zeng, L.S., Chen, S.Y., Li, H.B., Qi, X.X., Wooden, J.L., Mazdab, F.K., 2005. Characteristics of the granitoid complex and its zircon shrimp dating at the south margin of the Bashikaogong basin, north Altun, NW China. Acta Petrologica Sinica 21, 846–858 (in Chinese with English abstract).
Wu, F.Y., Yang, Y.H., Xie, L.W., Yang, J.H., Xu, P., 2006. Hf isotopic compositions of the standard zircons and baddeleyites used in U-Pb geochronology. Chemical Geology 234, 105–126.
Wu, C.L., Yao, S.Z., Zeng, L.S., Yang, J.S., Wooden, J.L., Chen, S.Y., Mazdab, F.K., 2007. Characteristics of the Bashikaogong-Simierbulake granitoid complex and its zircon SHRIMP dating in the northern Altun, NW China. Science in China: Series D 37, 10–26 (in Chinese with English abstract).
Wu, Y., Chen, Z.L., Chen, B.L., Wang, Y., Meng, L.T., He, J.T., Han, M.M., Wang, B., 2016. Geochronological and geochemical characteristics of the deformed diorite from the North Altyn brittle-ductile shear zone and its constraint on the Early Paleozoic tectonic evolution of the North Altyn Tagh. Acta Petrologica Sinica 32, 555–570 (in Chinese with English abstract).
Xiong, X.L., 2006. Trace element evidence for growth of early continental crust by melting of rutile-bearing hydrous eclogite. Geology 34, 945–948.
Xiong, X.L., Adam, J., Green, T.H., 2005. Rutile stability and rutile/melt HFSE partitioning during partial melting of hydrous basalt: implications for TTG genesis. Chemical Geology 218, 339–359.
Xiu, Q.Y., Yu, H.F., Liu, Y.S., Lu, S.N., Mao, D.B., Li, H.M., Li, Q., 2007. Geology and zircon U-Pb age of pillow basalt at Qiashikansoy in northern Altun Tagh, W China. Acta Geologica Sinica 81, 787–794 (in Chinese with English abstract).
Xu, Z.Q., Yang, J.S., Zhang, J.X., Jiang, M., Li, H.B., Cui, J.W., 1999. A comparison between the tectonic units on the two sides of the Altun sinistral strike-slip fault and the mechanism of lithospheric shearing. Acta Geologica Sinica 73, 193–205 (in Chinese with English abstract).
Xu, J.F., Shinjo, R., Defant, M.J., Wang, Q., Rapp, R.P., 2002. Origin of Mesozoic adakitic intrusive rocks in the Ningzhen area of east China: partial melting of delaminated lower continental crust? Geology 30, 1111–1114.
Xu, P., Wu, F.Y., Xie, L.W., Yang, Y.H., 2004. Hf isotopic compositions of the standard zircons for U-Pb dating. Chinese Science Bulletin 49, 1642–1648.
Yang, J.S., Shi, R.D., Wu, C.L., Su, D.C., Chen, S.Y., Wang, X.B., Wooden, J.L., 2008. Petrology and SHRIMP age of the Hongliugou ophiolite at Milan, north Altun, at the margin of the Tibetan plateau. Acta Petrologica Sinica 24, 1567–1584 (in Chinese with English abstract).
Yang, K.F., Fan, H.R., Santosh, M., Hu, F.F., Wilde, S.A., Lan, T.G., Lu, N.N., Liu, Y.S., 2012. Reactivation of the Archean lower crust: implications for zircon geochronology, elemental and Sr-Nd-Hf isotopic geochemistry of late Mesozoic granitoids from northwestern Jiaodong Terrane, the North China Craton. Lithos 146-147, 112–127.
Yang, H., Zhang, H.F., Luo, B.J., Zhang, J., Xiong, Z.L., Guo, L., Pan, F.B., 2015. Early Paleozoic intrusive rocks fromthe eastern Qilian orogen, NE Tibetan plateau: petrogenesis and tectonic significance. Lithos 224-225, 13–31.
Yu, S.Y., Zhang, J.X., Pablo García, D.R., Hou, K.J., Gong, J.H., Li, Y.S., 2013. Early-Neoproterozoic Grenvillian orogeny in Altun-Qilian-North Qaidam, North Tibet: new geochemical and zircon U-Pb and Lu-Hf isotopic constraints. Journal of Asian Earth Sciences 73, 372–395.
Yu, S.Y., Zhang, J.X., Qin, H.P., Sun, D.Y., Zhao, X.L., Cong, F., Li, Y.S., 2015. Petrogenesis of the early Paleozoic low-Mg and high-Mg adakitic rocks in the North Qilian orogenic

belt, NW China: implications for transition from crustal thickening to extension thinning. Journal of Asian Earth Sciences 107, 122–139.
Zen, E.A., 1986. Aluminum enrichment in silicate melts by fractional crystallization: some mineralogic and petrographic constraints. Journal of Petrology 27, 1095–1117.
Zhang, J.X., Meng, F.C., 2006. Lawsonite-bearing eclogites in the north Qilian and north Altyn Tagh: evidence for cold subduction of oceanic crust. Chinese Science Bulletin 51 (10), 1238–1244.
Zhang, J.X., Meng, F.C., Yang J., S., 2005. A new HP/LT metamorphic terrane in the northern Altyn Tagh, western China. International Geology Review 47, 371–386.
Zhang, S.H., Zhao, Y., Liu, X.C., Liu, D.Y., Chen, F.K., Xie, L.W., Chen, H.H., 2009. Late Paleozoic to Early Mesozoic mafic–ultramafic complexes from the northern North China Block: constraints on the composition and evolution of the lithospheric mantle. Lithos 110, 229–246.
Zhang, J.X., Mattinson, C.G., Yu, S.Y., Li, Y.S., 2014. Combined rutile-zircon thermometry and U-Pb geochronology: new constraints on Early Paleozoic HP/UHT granulite in the south Altyn Tagh, north Tibet, China. Lithos 200-201, 241–257.
Zhang, J.X., Yu, S.Y., Mattinson, C.G., 2015. Early Paleozoic polyphase metamorphism in northern Tibet, China. Gondwana Research (in press).
Zhao, X.F., Zhou, M.F., Li, J.W., Wu, F.Y., 2008. Association of Neoproterozoic A- and I-type granites in South China: implications for generation of A-type granites in a ubduction-related environment. Chemical Geology 257, 1–15.
Zhu, K.Y., Li, Z.X., Xu, X.S., Wilde, S.A., 2013. Late Triassic melting of a thickened crust in southeastern China: evidence for flat-slab subduction of the Paleo-Pacific plate. Journal of Asian Earth Sciences 74, 265–279.